Cell

Article

Circuit Design Features of a Stable Two-Cell System

Graphical Abstract

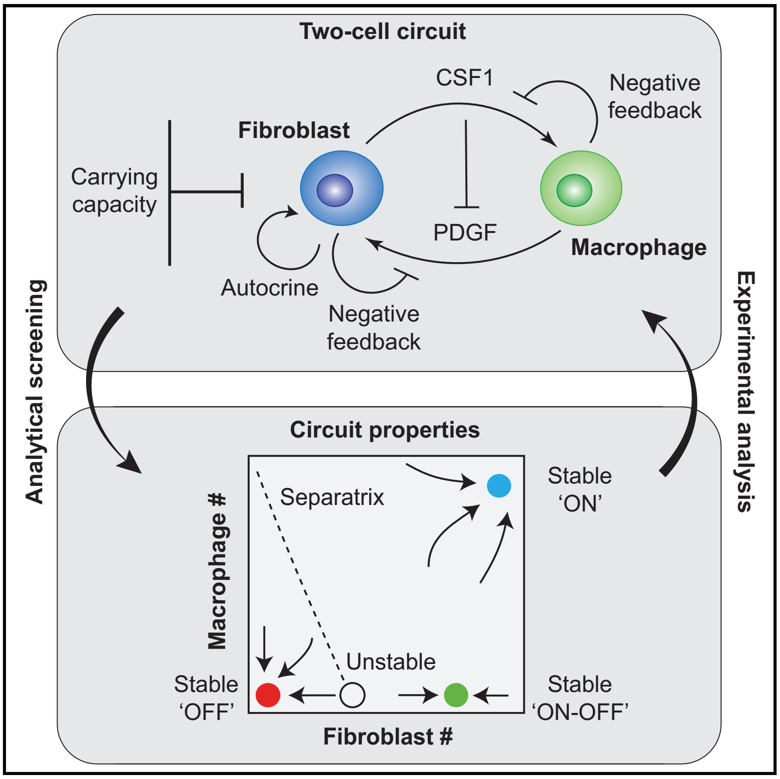

Highlights

- Macrophages and fibroblasts form a stable cell circuit resilient to perturbations
- Analytical screening reveals design principles for population stability
- The MP and FB circuit maintains stability through a "spring-and-ceiling" model
- Cell contact provides competitive advantage because of local exchange of growth factors

Authors

Xu Zhou, Ruth A. Franklin, Miri Adler, ...,
Avi Mayo, Uri Alon, Ruslan Medzhitov

Correspondence

uri.alon@weizmann.ac.il (U.A.),
ruslan.medzhitov@yale.edu (R.M.)

In Brief

How is the cellular composition of a tissue stably maintained?

Zhou et al., 2018, Cell *172*, 744–757
February 8, 2018
https://doi.org/10.1016/j.cell.2018.01.015

CellPress

Cell

Article

Circuit Design Features of a Stable Two-Cell System

Xu Zhou,[1,4] Ruth A. Franklin,[1,4] Miri Adler,[2,4] Jeremy B. Jacox,[1,3] Will Bailis,[1] Justin A. Shyer,[1] Richard A. Flavell,[1] Avi Mayo,[2] Uri Alon,[2,*] and Ruslan Medzhitov[1,5,*]

[1]Howard Hughes Medical Institute, Department of Immunobiology, Yale University School of Medicine, New Haven, CT 06510, USA
[2]Department of Molecular Cell Biology, Weizmann Institute of Science, Rehovot, 7610001, Israel
[3]Department of Internal Medicine, Yale University School of Medicine, New Haven, CT 06510, USA
[4]These authors contributed equally
[5]Lead Contact
*Correspondence: uri.alon@weizmann.ac.il (U.A.), ruslan.medzhitov@yale.edu (R.M.)

https://doi.org/10.1016/j.cell.2018.01.015

SUMMARY

Cell communication within tissues is mediated by multiple paracrine signals including growth factors, which control cell survival and proliferation. Cells and the growth factors they produce and receive constitute a circuit with specific properties that ensure homeostasis. Here, we used computational and experimental approaches to characterize the features of cell circuits based on growth factor exchange between macrophages and fibroblasts, two cell types found in most mammalian tissues. We found that the macrophage-fibroblast cell circuit is stable and robust to perturbations. Analytical screening of all possible two-cell circuit topologies revealed the circuit features sufficient for stability, including environmental constraint and negative-feedback regulation. Moreover, we found that cell-cell contact is essential for the stability of the macrophage-fibroblast circuit. These findings illustrate principles of cell circuit design and provide a quantitative perspective on cell interactions.

INTRODUCTION

Maintaining stability of cell populations is a key feature of metazoan tissues. Most tissues and organs contain multiple cell types and remain largely constant in size and cell composition under normal conditions (Raff, 1996). Alterations in tissue composition can occur during remodeling and inflammation, but are generally reversible (Nathan and Ding, 2010). However, sustained deviations are often associated with pathological conditions, such as chronic inflammation and degenerative and fibrotic diseases (Majno and Joris, 2004). How mammalian tissues maintain population homeostasis and how pathological deviations in cell composition are sustained remain poorly understood.

One way in which tissues maintain a stable population of cells is to regulate growth factor availability. Growth factors are required for cell survival and proliferation, and all normal (untransformed) cells undergo apoptosis upon growth factor deprivation (Raff, 1992). In a particular environment, a source of growth factor for a given cell can be either the same cell (autocrine signal) or, more commonly, a different cell type (paracrine signal) (Figure 1A) (Youk and Lim, 2014). The exchange of growth factors between two or more cell types establishes a cell circuit. In theory, even for the simplest two-cell circuits, there are numerous possible circuit topologies, given that the growth factor produced by either cell may control proliferation and/or growth factor production by the other cell. A cell circuit system may possess different properties such as stability and robustness, depending on the circuit topology (Hart et al., 2012; Karin and Alon, 2017; Karin et al., 2016; May, 1973). Earlier work has demonstrated such emerging properties using synthetic unicellular systems (Payne and You, 2014). However, the general principles of cell circuits in mammalian tissues have not been established. It is also not known what the properties and the quantitative characteristics of different cell circuit topologies are and which of the theoretically possible circuits are used in biological systems.

In addition to growth factor production, tissue composition can be controlled by extrinsic factors, such as oxygen, nutrient, and space availability. When considering population growth, these factors define the “carrying capacity” of the environment for a given cell type (Hart et al., 2014). Formally, carrying capacity is the maximum population size that can be supported in a given environment (Gotelli, 2008). When resources are not limiting, self-replicating populations can undergo periods of exponential growth, but as population size increases, inevitably some environmental factors become limiting and the growth rate progressively declines to zero when the population reaches its carrying capacity (Figure S1A). This pattern of population growth, known as logistic growth, is common in population dynamics, and its application to cell populations may yield important insights (Hart et al., 2014). Contact inhibition is a familiar example of an extrinsic limitation on cell growth *in vitro*. Within tissues, it is conceivable that carrying capacity may be similarly defined by spatial constraints. Interestingly, in the same tissue compartment, some cell types can be close to carrying capacity (e.g., most epithelia), while other cell types may be far from carrying capacity (e.g., leukocytes), thus enabling their transient expansion, as is the case for leukocytes during inflammation. However, it is unclear how stability of multiple cell types is established,

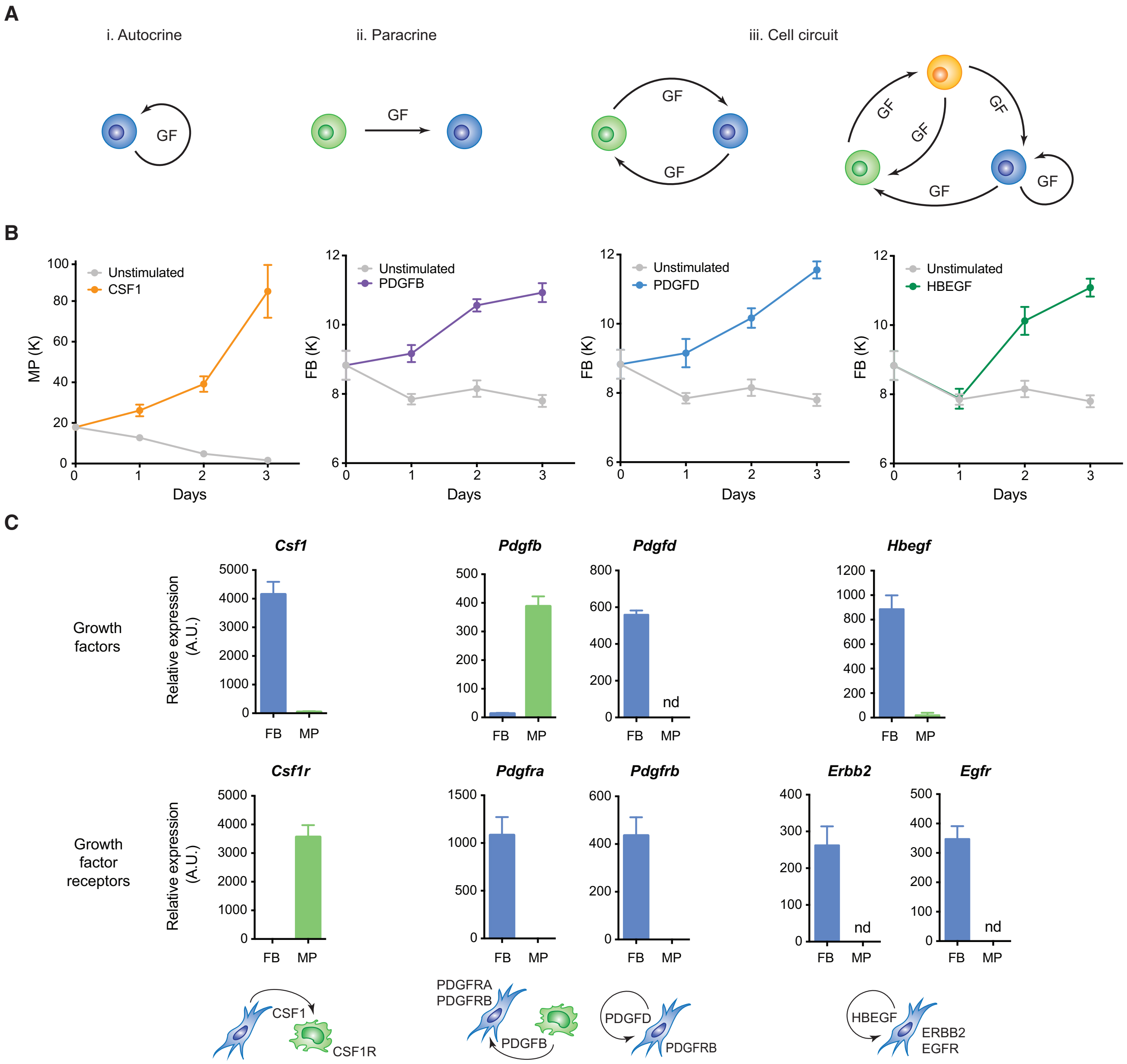

Figure 1. Reciprocal Expression of Growth Factors and Their Receptors Results in Proliferation of Macrophages and Fibroblasts

(A) Illustration of growth factor (GF)-dependent cell circuits.

(B) Growth factor-dependent proliferation of macrophages (MPs) and fibroblasts (FBs). MPs or FBs were fed daily with 50 ng/ml recombinant CSF1, PDGFB, PDGFD, or HBEGF. Cell numbers were determined each day starting 6 hr after plating (day 0) for 3 total days (data representative of three independent experiments, n = 7).

(C) Expression of growth factors and growth factor receptors in MPs and in FBs. RNA expression in MPs and in FBs was quantified by qPCR and normalized to *Hprt1* expression; nd, not detected (data representative of two independent experiments, n = 3).

Data are represented as mean ± SEM (B) or mean ± SD (C). See also Figure S1 and Table S1.

especially for cells that are maintained below their extrinsic limitations during homeostasis.

Given that growth factor availability controls cell survival and proliferation, we hypothesized that stability of cell composition can be maintained by cell circuits based on growth factor exchange. Traditional genetic models have demonstrated that the presence of different cell types within tissues is dependent on growth factors (Trapnell and Whitsett, 2002; Wiktor-Jedrzejczak et al., 1990). Because *in vivo* genetic models are not well suited for quantitative and mechanistic analyses, we employed an *in vitro* system to analyze a minimal two-cell circuit in which the two cell types can be the source of growth factors for each

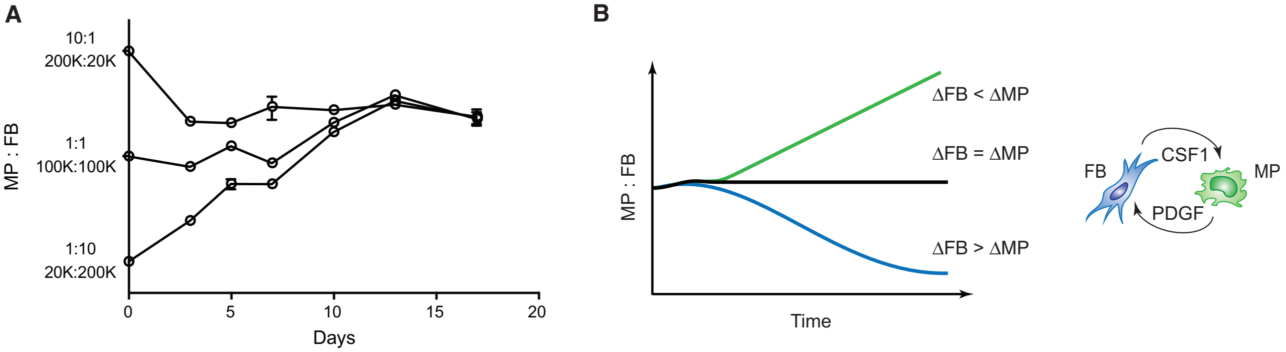

Figure 2. Co-cultures of Macrophages and Fibroblasts Reach Stable Cell Ratios

(A) Time course of population ratios for MPs and FBs in co-culture. MPs and FBs were plated with starting ratios spanning a range of up to 100-fold. Ratios over time were calculated using flow cytometry (data representative of five independent experiments, n = 2).

(B) Simulated population ratios of a growth factor-dependent cell circuit. ΔFB and ΔMP are net changes in population size (proliferation − removal).

Data are represented as mean ± SD. See also Figure S2 and Movie S1.

other. We used macrophages and fibroblasts, as these cell types are found in almost all mammalian tissues and perform important homeostatic functions, including growth factor production (Davies et al., 2013; Guilliams and Scott, 2017; Okabe and Medzhitov, 2016; Wynn, 2008). We found that macrophages and fibroblasts do indeed form a two-cell circuit through exchange of growth factors. The macrophage-fibroblast circuit is stable and resilient against aberrant proliferation or transient macrophage expansion, presenting features similar to mammalian tissues. The system also revealed an unexpected contact-dependent mechanism of growth factor exchange required for population stability. Finally, by using analytical modeling to screen all possible two-cell circuit topologies used by macrophages and fibroblasts, we described quantitative characteristics and the features required for cell circuit stability.

RESULTS

Macrophages and Fibroblasts Constitute a Two-Cell Growth Factor Circuit

To establish an *in vitro* system for the investigation of circuit stability, we tested whether murine bone marrow-derived macrophages (hereafter macrophages or MPs) and murine embryonic fibroblasts (hereafter fibroblasts or FBs) could communicate through growth factor production and detection. By examining pairs of growth factors and growth factor receptors that are highly expressed in either macrophages or fibroblasts (Figures S1B and S1C), we found four growth factors with the potential to support proliferation of either macrophages or fibroblasts (Figure 1B and S1D). These growth factors and their receptors constitute three possible connections between macrophages and fibroblasts (Figure 1C; Table S1). First, fibroblasts express high levels of *Csf1*, while the CSF1 receptor (*Csf1r*) is exclusively expressed on macrophages. This lineage-restricted growth factor is required for macrophage survival and proliferation (Figure 1B) (Chitu and Stanley, 2006). Second, macrophages have high PDGF (*Pdgfb*) expression, and both PDGF receptors, *Pdgfra* and *Pdgfrb*, are exclusively expressed on fibroblasts. PDGF family members are critical growth factors for survival and proliferation of stromal cells, including fibroblasts (Andrae et al., 2008; Heldin and Westermark, 1999). Therefore, growth factors produced from macrophages also promote proliferation of fibroblasts. Third, we observed a possible autocrine loop for fibroblasts via members of the PDGF (*Pdgfd*) and EGF (*Hbegf*) families. Such positive feedback may support fibroblast survival or expansion in the absence of other growth factor sources. These three possible growth factor connections constitute a macrophage-fibroblast circuit (Figure 1C). In addition, macrophages isolated directly from mouse tissues also express high levels of *Pdgfb* and *Csf1r in vivo* (Figure S1E) (Lavin et al., 2014), suggesting physiological relevance of these growth factor interactions.

Macrophages and Fibroblasts Establish a Stable Cell Circuit

Animal tissues normally maintain stable cell composition, which is governed by the local provision of growth factors. Since macrophages and fibroblasts show reciprocal expression of their requisite growth factors and growth factor receptors (Figure 1C), we asked whether a two-cell system composed of macrophages and fibroblasts is sufficient to reach population stability. The two cell types are both adherent and maintain physical contact throughout the course of population growth (Figure S2A). We mixed the two cell types with initial ratios spanning a range of up to 2,500-fold and followed the kinetics of both populations by flow cytometry (Figure S2B). Strikingly, over a 2-week period, the two cell types reached a stable ratio (Figures 2A, S2C, and S2D). In addition, macrophages and fibroblasts could each converge to stable numbers (Figure S2D). Because of variation in the proliferative capacity of primary cells, we found that ratio serves as a more robust measurement of stability. This stability between two cell types is not trivial in that it implies a mechanism(s) that prevents runaway growth for either cell type. Indeed, if both cell types simply produced growth factors for each other, cell proliferation would result in an increase in growth factors and an increase in both cell types. In this scenario, a stable population ratio would only be achieved if the two cell types expanded exactly proportionally (Figure 2B). Therefore,

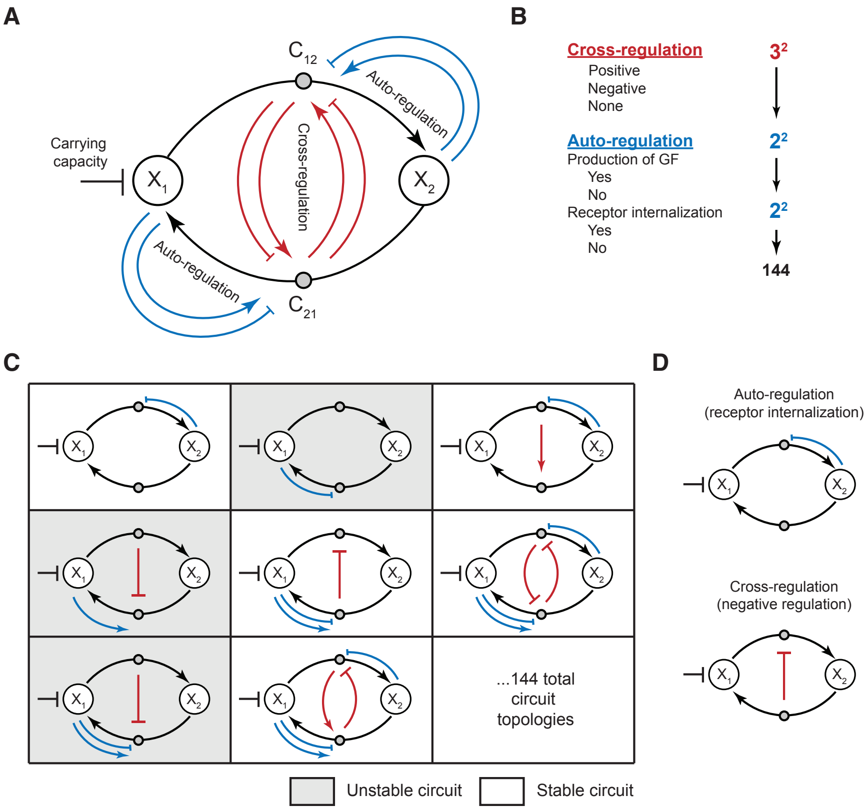

Figure 3. Analytical Screening Identifies Negative Feedback as a Necessary Feature of a Stable Two-Cell Circuit

(A) Illustration of analytical screening of a growth factor-dependent circuit. X_1 is cell 1; X_2 is cell 2; C_{12} is the growth factor made by X_1 for X_2; and C_{21} is the growth factor made by X_2 for X_1. Red and blue arrows indicate different forms of regulation on growth factors.

(B) Enumeration of all possible circuit interactions in the analytical screen resulted in 144 different circuit topologies.

(C) Examples of both stable and unstable two-cell circuits identified by the screen.

(D) Two minimal circuits that generate circuit stability. Both circuits show negative feedback on cell X_2, in which cell X_2 effectively downregulates its own growth factor, either by auto-regulation (top) or by cross-regulation (bottom).

See also Figure S3.

additional mechanisms coordinating cell proliferation and/or growth factor production are required to support circuit stability.

Analytical Screening Shows Principles for Population Stability

To identify the circuit properties that could result in population stability in a two-cell system, we used an analytical screening approach of mathematical models of two-cell circuits (for details of the modeling, see Adler et al., 2018). We defined X_1 and X_2 as the concentrations of the two cell types and C_{12} and C_{21} as the concentrations of the growth factors made by one cell type and received by the other (e.g., C_{12} is the growth factor made by cell X_1 for cell X_2) (Figure 3A). When neither cell type is limited by circuit-extrinsic mechanisms, cells grow exponentially, and the system is unstable no matter what additional cell circuit regulation is in place (Figure S3A). When both cell types are constrained by the environment, cells grow until they approach their respective environmental limitation without the need for additional regulation (Figure S3B). In this case, the stable state is primarily defined by the environment rather than the cell circuit itself. Most interestingly, the system can reach stability if only one cell type is limited by the carrying capacity of the environment (Figure S3C). This stability requires regulation of growth factor availability or responsiveness and depends on intrinsic properties of the circuits (Adler et al., 2018).

Growth factors within a two-cell circuit can be regulated through cross-regulation (one cell type to the other) or auto-regulation (one cell type to itself) (Figure 3A). For cross-regulation (red), the growth factor secreted by one cell type can positively or negatively affect the production of the growth factor secreted by the other cell type. This regulation may include mechanisms that change the overall protein expression of growth factors via mRNA transcription, protein synthesis, and/or protein secretion. For auto-regulation (blue), a given cell type regulates the availability of the growth factor for itself, through mechanisms regulating growth factor production or growth factor removal. The most common mechanisms are autocrine growth factor production (Citri and Yarden, 2006) and removal of growth factors through receptor-mediated endocytosis (Goh and Sorkin, 2013).

With this in mind, we generated all 144 possible two-cell circuit topologies according to the following interactions (Figure 3B): (1) three possibilities for cross-regulation (positive, negative, or absent); (2) two possibilities for production of growth factors: each cell type can or cannot produce a growth factor for its own growth and survival; and (3) two possibilities for internalization of growth factors: each cell type can or cannot remove its growth factor by receptor-mediated endocytosis. Each topology also has molecular rate parameters, such as growth factor lifetimes, internalization rates, cell division and removal rates, and growth factor affinities (Table S2). To solve the circuit dynamics, stability, and robustness for all possible parameters, we modeled these circuits considering all possible interactions (Adler et al., 2018).

We find that 48 of these 144 topologies allow a stable steady state for a wide range of parameters. Each parameter, such as growth factor production and consumption rates, and cell removal and proliferation rates, can vary by at least 10-fold around a biologically plausible value and stability is still maintained. These circuits all show an "ON" state in which the concentrations of the two cell types flow to a stable coexistence at a prescribed ratio, from a wide range of initial conditions. These circuits also show an "OFF" state in which cells at low concentration decay to zero. This phenomenon, when a population does not grow unless it has critical density is known in ecology as "Allee effect," and the minimal population density as "Allee number" (Figure S1A) (Gotelli, 2008). 24 of these 48 circuits show a third steady-state fixed point: an "ON-OFF" state in which one cell type is present in the absence of the other (supported by an autocrine loop; Figures 1C and S3D). The remaining 96 topologies either can never show a stable ON state for any parameter set (60/144) or can show a stable ON state for only a very restricted range of parameters (36/144). This screen thus demonstrates the feasibility of a steady-state co-existence of two cell types through growth factor interactions ("ON" state), when one cell type is close to carrying capacity. In this case, a necessary and sufficient condition for a stable "ON" state is that the growth factor of the cell far from carrying capacity must undergo negative regulation (either by internalization or cross-repression) (Figure 3D) (Adler et al., 2018). This requirement is found in all of the 48 circuits in the screen which showed a stable "ON" state. We name this mechanism for stability the "spring-and-ceiling" model. The ceiling is the carrying capacity that keeps one cell type from expanding. The spring is the negative regulation of the growth factor for the other cell type. This negative regulation connects the two cell types like a spring and anchors the cell type far from its carrying capacity at a finite concentration, thus preventing overexpansion (Figure S3C).

The Macrophage-Fibroblast Circuit Maintains Stability through Negative Regulation of CSF1

Next, we tested the "spring-and-ceiling" model prediction that (1) one cell type is close to carrying capacity and (2) the other has negative feedback on its growth factor availability. We first examined the "ceiling," and asked: which cell type is constrained by carrying capacity? Carrying capacity K is defined as the cell number where the proliferation rate is zero. The expansion of a cell population gradually approaching its carrying capacity can be described with a logistic growth function, where proliferation rate negatively correlates with cell density when a population approaches carrying capacity (Figure 4A).

We devised an approach to experimentally estimate the value of carrying capacity for any cell type by quantifying the relationship between proliferation rate and population size. The linear intercept of proliferation rate with the x axis, namely the cell number at which the proliferation rate reaches zero, is the carrying capacity for that cell type. In this assay, EdU-labeling identifies dividing cells, thus EdU% is used as an approximation for proliferation rate. As proof of principle, we measured carrying capacity of fibroblasts in tissue culture wells of different areas. Doubling the area of the well doubled the cell number at which proliferation reached zero, suggesting that in this setting, carrying capacity is proportional to space (Figure S4A). Using this system, we further observed that fibroblast proliferation is negatively correlated with cell density, whereas macrophage proliferation is largely density independent (Figures 4B, S4D, and S4E). This demonstrates that fibroblasts, but not macrophages, are limited by carrying capacity.

The present approach also allowed us to quantitatively dissect changes in carrying capacity and proliferation. Varying the available space only changed carrying capacity, but not proliferation (Figure S4A), whereas varying nutrient levels altered both carrying capacity and cell proliferation (Figure S4B). However, altering nutrient levels in the co-culture did not affect system stability, as macrophage to fibroblast ratios were similar in co-cultures regardless of serum concentration (Figure S4C). Macrophages showed enhanced proliferation in response to recombinant CSF1 (Figures S4D and S4F), while fibroblasts exhibited a significant increase in both carrying capacity and cell proliferation in response to recombinant PDGFB (Figures S4E and S4F). These data suggest that carrying capacity is a cell type-specific property even though both cell types are exposed to the same system environment. The suppression of fibroblast proliferation upon reaching carrying capacity could be regulated through contact inhibition *in vitro* and by mechanisms controlling organ size *in vivo*, such as the Hippo pathway (Yu et al., 2015).

Next, we asked about the "spring" in the predicted "spring-and-ceiling" model: is the growth factor for the cell far from carrying capacity negatively regulated through either internalization or cross-repression? First, we investigated if internalization of either CSF1 or PDGFB plays a major role in their removal. After growth factor binding, removal of growth factors from the environment through internalization of growth factor receptors has been well documented (Goh and Sorkin, 2013). CSF1 binds to CSF1 receptor (CSF1R) and PDGFB binds to both PDGF receptors (PDGFRA/PDGFRB). Therefore, we tested if CSF1R or PDGFRA/B internalization allows for depletion of CSF1 or PDGFB. After stimulation with growth factors, the surface expression of receptors for CSF1 and PDGFB decreased within minutes ($t_{1/2}$ ~1.5 min for CSF1R, $t_{1/2}$ ~3–6 min for PDGFRA/B) (Figures 4C and S4G). Furthermore, the available growth factors in the supernatant were quickly depleted (Figure S4H). These data suggest that internalization is the dominant mechanism for removal of both CSF1 and PDGFB.

Next, we examined if cross-regulation of either growth factor occurs. We did not observe cross-regulation of CSF1: expression of *Csf1* in fibroblasts was not influenced by exogenous PDGFB (Figure 4D). Conversely, we observed cross-regulation in the other direction: exogenous CSF1 downregulated the expression of *Pdgfb* in macrophages. Interestingly, modeling suggests that this cross-regulation does not significantly affect the dynamics, since fibroblasts are mainly regulated by their carrying capacity. However, this feature might be important in different contexts, when fibroblasts are transiently unconstrained by carrying capacity, for example, during tissue repair.

In summary, the regulation of cell growth in the macrophage-fibroblast system includes the following regulatory interactions: fibroblast proliferation is limited by carrying capacity but macrophage proliferation is not, CSF1 and PDGFB removal occurs mainly through receptor internalization, and CSF1 downregulates *Pdgfb* mRNA expression in macrophages (Figure 4E). Thus, we experimentally demonstrate the two features minimally required for spring-and-ceiling circuit stability as predicted by modeling: (1) fibroblasts are limited by carrying capacity (ceiling) and (2) the growth factor for macrophages, CSF1, is negatively regulated through receptor internalization (spring). This

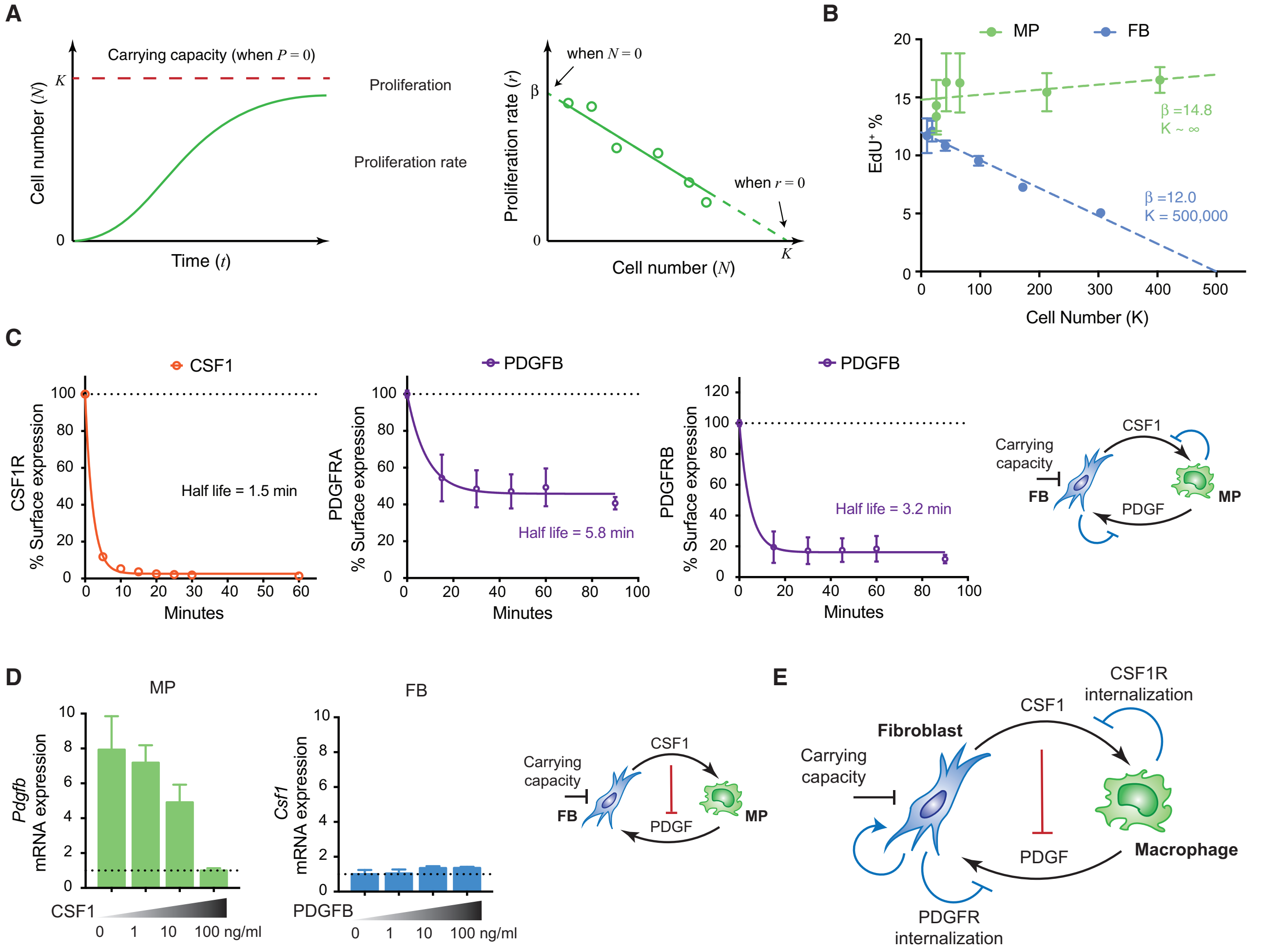

Figure 4. Circuit Stability Is Maintained through Carrying Capacity and Negative Regulation

(A) Mathematical definition of carrying capacity. The growth curve of cell number N is modeled with maximum proliferation rate β, carrying capacity K, and cell removal rate μ.

(B) Measurement of carrying capacity for MPs and FBs. Proliferation rate was approximated using the percentage of EdU$^+$ cells after overnight culture and 2 hr of EdU labeling. MPs and FBs were plated at different cell densities range from 10,000 to 500,000 in 6-well plates. Actual cell numbers at the time of assay are depicted. Carrying capacity (K) and proliferation rate (β) were determined as the intercepts of the x and y axes with linear fit. (Data are representative of three independent experiments, n = 3.)

(C) Relative surface expression of CSF1 receptor on MPs and PDGF receptors on FBs after growth factor stimulation with 50 ng/ml CSF1 or 50 ng/ml PDGFB as measured by flow cytometry. (Data are representative of two independent experiments, n = 3.)

(D) Expression of *Pdgfb* in MPs and *Csf1* in FBs after addition of 50 ng/ml CSF1 and 50 ng/ml PDGFB for 24 hr. RNA expression was quantified by qPCR and normalized to *Hprt1* expression. (Data are representative of two independent experiments, n = 3.)

(E) Model depicting the MP-FB circuit, including carrying capacity, reciprocal growth factor expression, negative feedback through growth factor receptor internalization and transcriptional suppression, and autocrine growth factor production by FBs.

Data are represented as mean ± SEM (B and C) or mean ± SD (D). See also Figure S4.

internalization ensures that if there are too many (or too few) macrophages, the rate of Csf1 removal increases (or decreases), returning the circuit back to steady state.

The Macrophage-Fibroblast Circuit Explains Population Dynamics

Circuit topologies not only determine the stability of a system but also determine (along with the rate parameters) how cells within a system proceed from one condition dynamically toward the next. This information can be summarized in a *phase portrait* depicting overall dynamic features of a system, with arrows marking the flow from one configuration to the next (Figure 5A). Phase portraits of the stable cell circuits we analyzed display both “ON” and “OFF” states (Figures 5A and 5B). Each of these states has a basin of attraction, a region in which cell dynamics flow toward that state. The basins are separated by a separatrix (dashed line) representing the boundary in which the dynamics switch between these two states (Figures 5A and 5B). In the circuit that we experimentally identified (Figure 4E), we also expect a third “ON-OFF” state, where one cell type (fibroblasts) can

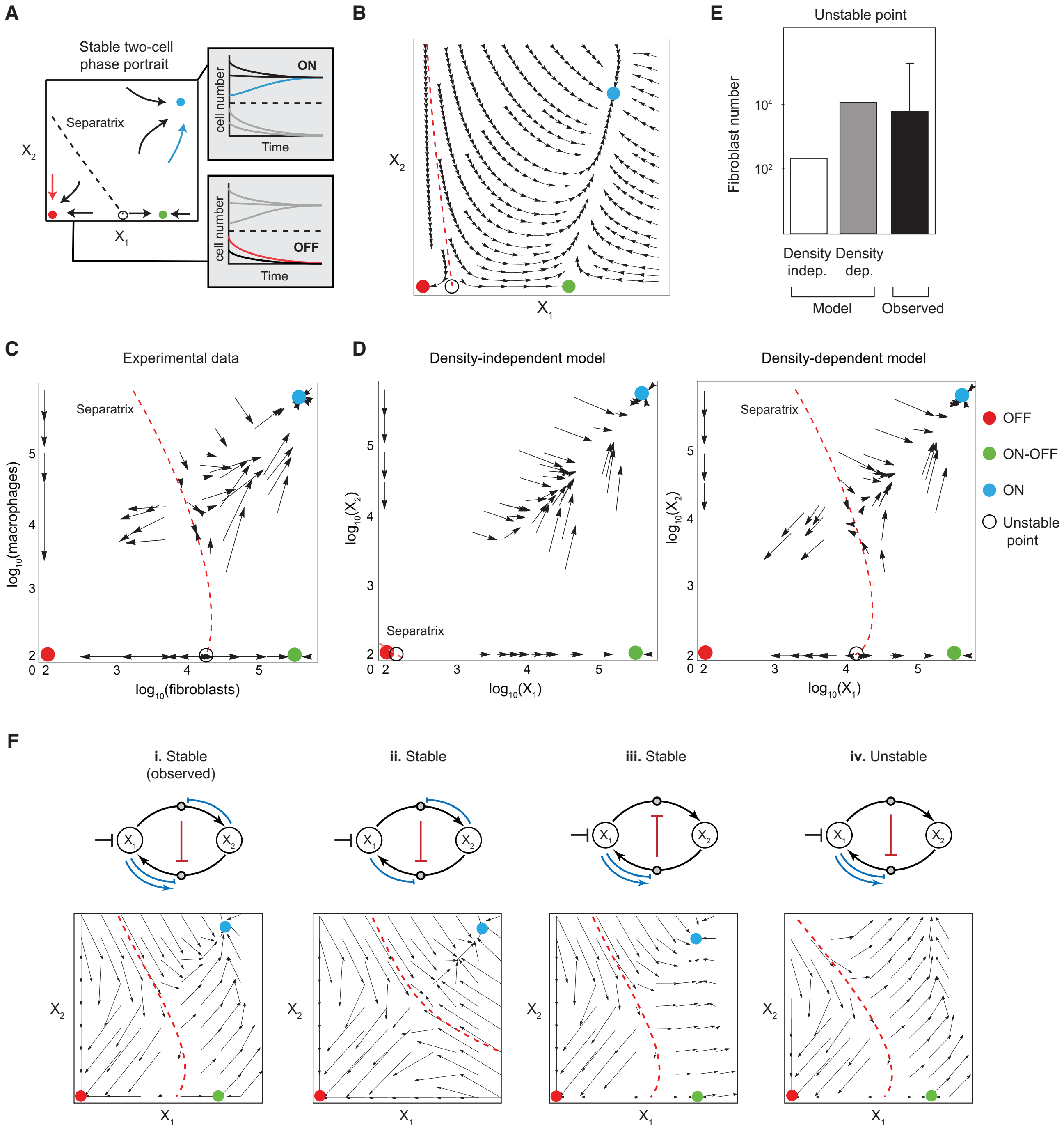

Figure 5. The Observed Stable Circuit Is Density Dependent

(A) Stable two-cell phase portrait showing "ON," "OFF," and "ON-OFF" states.

(B) Theoretical phase portrait depicting population kinetics.

(C) Phase portrait depicting MP-FB system kinetics measured *in vitro*. Each arrow tail represents one measurement 2 days after co-culture at a given starting cell number, and each arrowhead represents the cell numbers from this same condition 2–5 days later (54 separate conditions, n = 2). The separatrix represents the switch between the "ON" (blue circle) and "OFF" (red circle) states. The base of the separatrix is the unstable point (empty circle), where FB culture alone will either flow to the "ON-OFF" (green circle) or to the "OFF" state.

(D) Theoretical phase portraits using density-independent (left) and density-dependent (right) models, with identical model parameters (Table S2).

(E) Estimated values of the unstable points, empty circles in (D), from experimental observations (black bar) and density-independent and -dependent models (empty and gray bar).

(legend continued on next page)

reach stability in the absence of the other, due to an autocrine loop (Figures 1C, 5A, and 5B).

To produce an experimental phase portrait displaying cell circuit dynamics, we combined flow cytometry and fluorescent imaging to quantify the number of macrophages and fibroblasts at different time points, covering cell densities ranging across three orders of magnitude. Satisfyingly, the three stable states and the population dynamics of macrophages and fibroblasts in co-culture can be observed in this phase portrait (Figure 5C). As expected, macrophages do not survive without growth factors produced from fibroblasts (“OFF” state) (Figure 5C). When the system only contains fibroblasts, there are two stable states: if fibroblasts are below a certain threshold density (the Allee number or unstable point), the system eventually collapses (“OFF” state), and if fibroblasts are above the threshold density, they proliferate until limited by the environment (“ON-OFF” state). Consequently, macrophages and fibroblasts co-cultured together can be in two stable states: an “OFF” state in which cells cannot support sustained proliferation and an “ON” state in which the two cell types reach a stable point.

The observed dynamics thus qualitatively match the prediction from the cell-circuit model with the experimentally defined interactions. To determine whether the observed dynamics also match the predictions quantitatively, we compared the theoretical to the experimental phase portraits using biologically plausible values for the rate parameters to avoid overfitting the model (Table S2). The experimental phase portrait differs from the model with regards to the size of the basin of attraction of the “OFF” state: in the model the basin is very small, with most conditions resulting in attraction to the “ON” state (Figure 5D, left), while the data show a larger basin of attraction to the “OFF” state, with the unstable point on the x axis (empty circle) higher by two orders of magnitude. Since macrophages and fibroblasts associate with each other throughout the co-culture (Figure S2A; Movie S1), we hypothesized that this difference could be explained by density-dependent effects; for example, if growth factor exchange occurs locally, or if the growth factor diffusion range is less than the distance between cells. To account for such effects, we replotted the model phase portrait using rescaled concentration axes. We used a simple Poisson model to rescale the concentration according to the probability of cells to be in proximity (see the STAR Methods). Interestingly, the model and experimental phase portraits are very similar when cell density is taken into consideration. We observe comparable positions of the unstable point and separatrix, and sizes of the basin of attraction (Figures 5D, right, and 5E). This agreement is largely insensitive to changes in model parameters (Table S3). Varying parameters preserves the structure of the phase portrait and only moderately shifts the positions of the fixed points and the separatrix (Figures S5A–S5E). This density-dependent effect suggests that cell-cell contact between macrophages and fibroblasts may be important for stability of the cell circuit.

In addition to the circuit that we identified experimentally, several other circuit topologies can generate stable systems with distinct features. As further demonstration of the regulatory mechanisms identified in the macrophage-fibroblast circuit, theoretical phase portraits of circuits lacking key interactions were generated and the dynamics compared to the observed circuit (Figure 5F, “i”). Circuit “ii” is missing the autocrine signaling for fibroblasts, resulting in loss of the “ON-OFF” state. This circuit has a large basin of attraction to the “OFF” state and thus a less stable “ON” state. Circuit “iii” depicts a circuit with stability provided through cross-repression instead of auto-repression, which requires 8-fold more time to reach the stable “ON” state (Figure S5F) (Adler et al., 2018). Lastly, when negative feedback through receptor internalization is removed from the observed circuit (circuit “iv”), the “ON” state of the system becomes unstable and macrophages expand uncontrollably.

Modeling of these and other two-cell circuits demonstrate the importance of the identified circuit interactions (Figure 3). Since we did not distinguish between each specific mechanism that could be present in the system, other forms of regulation may contribute to macrophage-fibroblast interactions. These may include changes in growth factor synthesis, secretion, or processing, in addition to the mechanisms we directly tested. However, by comparing the kinetics of different circuits with our experimental observations, we can discern the regulation that is most relevant to the macrophage-fibroblast cell circuit.

The Macrophage-Fibroblast Circuit Is Resilient to Perturbations

The circuit model predicts that the macrophage-fibroblast system is resilient to perturbations, such as abrupt changes in growth factor concentrations or cell numbers (e.g., inflammatory infiltrate). To test this experimentally, we allowed the co-culture to reach stability and then introduced perturbations by supplementing with recombinant CSF1, PDGFB, or additional macrophages. Addition of CSF1 strongly biased the system toward macrophages by over 20-fold after 3 days, but the stable population ratio was restored after 3 weeks of co-culture (Figure 6A). Similar results were observed after the addition of macrophages. In response to PDGFB, the fibroblast population nearly doubled and then returned to the initial stable state in accordance with the transient increase in carrying capacity by growth factors (Figure S4E). Interestingly, macrophage numbers also increased in response to exogenous PDGFB due to expansion of the source of CSF1, resulting in an unchanged macrophage to fibroblast ratio. We observed similar behavior in the model simulations using corresponding changes in growth factor concentration and macrophage number (using the same model parameters as Figure 5) (Figure 6B). In both model and experiment, CSF1 addition mainly affected macrophage number and MP:FB ratio, whereas PDGFB addition mainly affected fibroblast number, with all effects eventually returning to baseline. Some

---

(F) Theoretical phase portraits of cell circuits with variations on the observed circuit (i): (ii) the observed circuit missing autocrine signaling for FBs (X_1); (iii) Circuit with stability provided through cross-repression of growth factor produced from X_1 instead of X_2; and (iv) negative feedback through receptor internalization removed from the observed circuit.

Data are represented as mean ± SD. See also Figure S5 and Table S3.

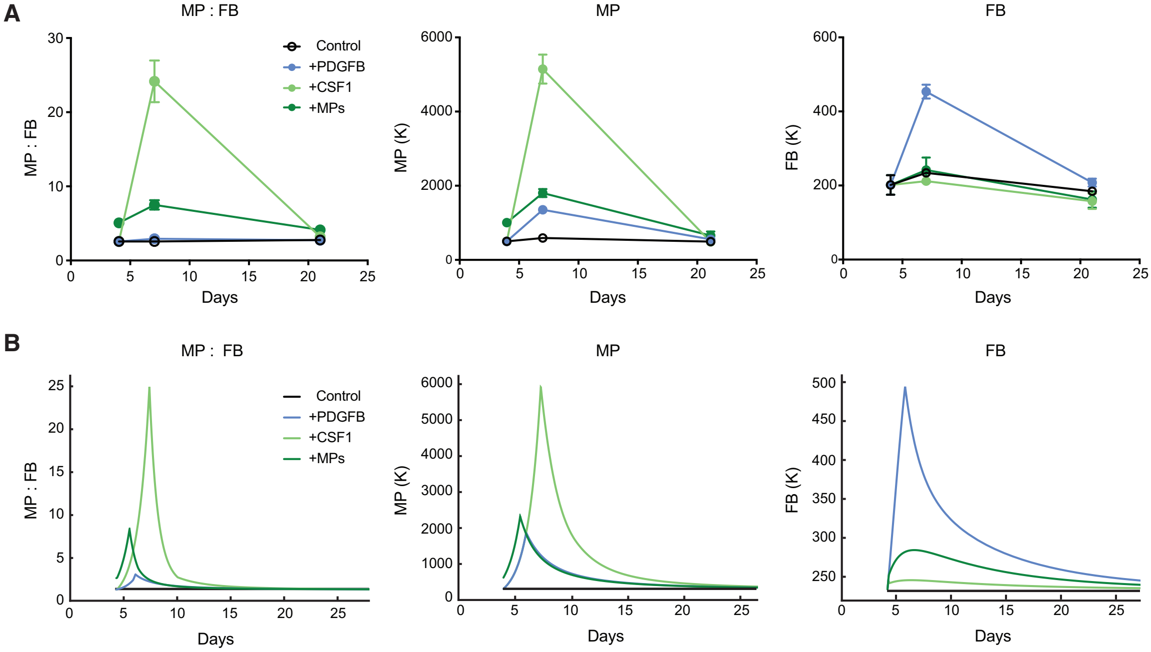

Figure 6. The Macrophage-Fibroblast Circuit Is Resilient to Perturbations

(A) Perturbation of MP-FB co-culture with the addition of recombinant CSF1, PDGFB, or MP. The population ratios (left), number of MPs (middle), and number of FBs (right) are shown for days 4, 7, and 21 of co-culture. On day 0, 100,000 FBs and 200,000 MPs were plated for co-culture. On day 4, a single dose of 50 ng/ml PDGFB, 50 ng/ml CSF1, or 500,000 MPs was added to co-culture. (Data are representative of two independent experiments, n = 3.)

(B) Dynamics of cell numbers and ratios after modeling the same perturbations experimentally performed in (A), using similar parameters from the phase portrait in Figure 5C (Table S2; STAR Methods).

Data are represented as mean ± SD.

quantitative discrepancies between model and data exist and warrant further testing at higher temporal resolution. Together, these results demonstrate that the macrophage-fibroblast system is resilient to perturbations.

Circuit Stability Requires Growth Factor Exchange

Since the density threshold that distinguishes the “OFF” and “ON-OFF” states depends on the proliferation of fibroblasts, the circuit model predicts that growth and stability of the fibroblast population relies on the presence of macrophages due to their production of PDGFB. Accordingly, we found that when fibroblasts were seeded below the Allee number, they only expanded when macrophages were present, moving the experimental condition from one side of the separatrix (flowing to the “OFF” state), to the other side of the separatrix (flowing to the “ON” state) (Figure 7A). Therefore, macrophages are required for robust fibroblast proliferation when fibroblast density is near their Allee number.

Next, we examined whether macrophage production of PDGFB was specifically required for this effect. When fibroblasts were plated below the unstable point, they expanded in the presence of wild-type macrophages (Figure 7B). However, when fibroblasts were cultured with PDGFB-deficient macrophages, fibroblasts failed to expand. As predicted by the model, macrophages play a more profound role in maintaining circuit stability below the unstable point. If fibroblasts were plated above the unstable point, they expanded regardless of whether or not macrophages were providing PDGFB (Figure S6A).

This requirement for paracrine growth factor production is also important for macrophages because they die in the absence of fibroblasts (Figure 5C). This implies that a stable two-cell system should collapse if fibroblasts are unable to produce CSF1. To test this, we deleted *Csf1* from fibroblasts (*Csf1* knockout [*Csf1*^{KO}]) (Figure S6B). When macrophages were cultured with *Csf1*^{KO} fibroblasts, both macrophages and fibroblasts failed to expand (Figure 7C). In contrast, when cultured with *Csf1*^{WT} fibroblasts, macrophages could proliferate, and both cell types expanded.

Cell-Cell Contact Allows for Local Exchange of Growth Factors

We also observed that the physical association between macrophages and fibroblasts depends on CSF1 (Figure 7D). Interestingly, macrophages were found in close contact with CSF1-sufficient fibroblasts, but not with CSF1-deficient cells. The macrophage-fibroblast contact was also observed throughout the length of culturing (Figure S2A). To understand more about the spatial relationship between macrophages and fibroblasts, we tracked their interactions using live cell imaging. Surprisingly, we observed long-term associations between the two cell types at both low and high densities, often for the full 14-hr duration of the movie (Figure 7E; Movies S1 and S3). At low cell density, macrophage velocity increased as the cells moved closer to

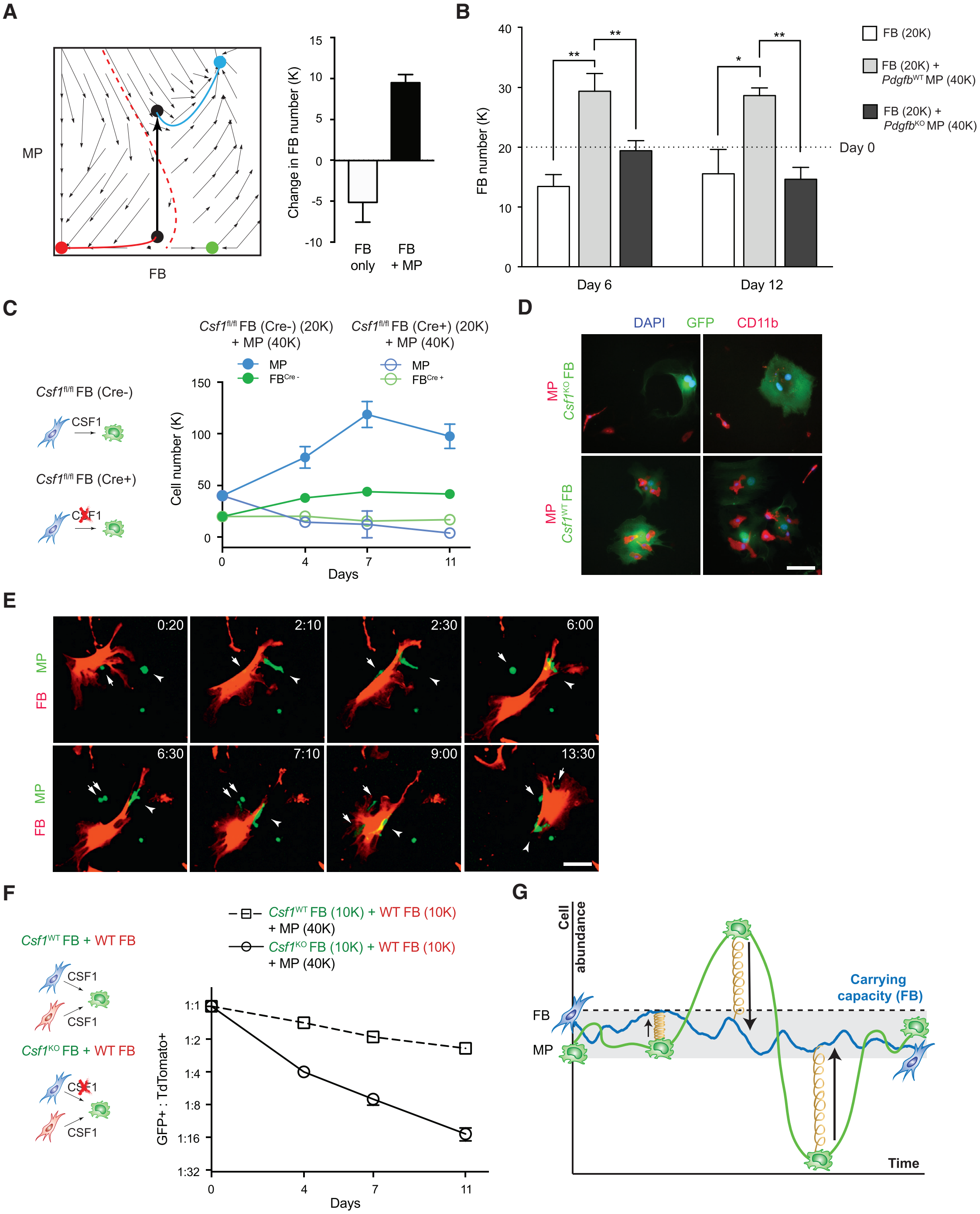

Figure 7. Stable Growth of Macrophages and Fibroblasts in Co-culture Requires Contact-Dependent Mechanisms

(A) A theoretical phase portrait showing the change in FB fate when cultured near the unstable point, with or without MPs (left). FB number when cultured with or without MPs (right). 20,000 FBs were cultured with 40,000 MPs, and cell numbers were evaluated on day 4 using flow cytometry. (Data are representative of two independent experiments, n = 3.)

(B) Co-cultures of FBs with *Pdgfb* WT or *Pdgfb* KO MPs. Cas9 knockin MPs transduced with lentivirus carrying empty vector (control) or vector carrying *Pdgfb* guides (*Pdgfb* KO) were plated together with FBs. On day 0, 20,000 FBs and 40,000 MPs were plated and the co-cultures were examined after 6 and 12 days. (Data are representative of two independent experiments, n = 3.)

(C) Co-cultures of MPs with control or *Csf1* KO FBs. *Csf1*$^{fl/fl}$ FBs transduced with lentivirus carrying GFP (control) or Cre-GFP (*Csf1* KO) were plated together with MPs. On day 0, 20,000 FBs and 40,000 MPs were plated, and the co-cultures were examined after 4, 7, and 11 days. (Data are representative of two independent experiments, n = 3.)

(legend continued on next page)

fibroblasts, capturing the "jumping" motion of macrophages onto growth factor-producing fibroblasts (Figure S6C; Movies S2 and S3). At high density, macrophages remain largely associated with the same fibroblasts (Movie S1). These observations further confirm the significance of cell-cell contact predicted by the comparison of the model to the experimental phase portrait (Figures 5C and 5D).

Next, we tested whether physical association between fibroblasts and macrophages is required for growth factor exchange. If physical interactions between macrophages and fibroblasts are necessary for co-culture stability, then CSF1-producing fibroblasts should show a growth advantage compared to non-producers. To this end, we mixed *Csf1*^{KO} or *Csf1*^{WT} fibroblasts (GFP$^+$) with wild-type (WT) fibroblasts (TdTomato$^+$) in equal numbers and co-cultured them with macrophages. We found that WT fibroblasts showed a significant advantage over *Csf1*^{KO} cells (Figures 7F and S6D), and that the relative abundance of *Csf1*^{WT} and WT fibroblasts remained stable. In fact, the remaining *Csf1*^{KO} fibroblasts made up less than 7% of the overall fibroblast population. This suggests that growth factors can act in a contact-dependent manner to support stable growth of macrophages and fibroblasts, with cells collapsing if they are not in contact with a growth-factor-producing cell.

DISCUSSION

Growth factors are required for metazoan cell proliferation and survival. In mammals, the source and recipient of these factors are often different cell types. Using primary murine macrophages and fibroblasts, we reconstituted a growth factor circuit where these two cell types exhibit reciprocal growth factor exchange. The resulting cell circuit recapitulates some features of mammalian tissues such as population stability and resilience against perturbations. Through analytical screening of circuit topologies, we identified the minimal circuits required for system stability and validated them experimentally. This analysis revealed that extrinsic restriction on the cell number of one cell type combined with negative-feedback regulation on the growth factors needed by the other cell type is sufficient for system stability. We termed these requirements the "spring-and-ceiling" model (Figure 7G). Further, we demonstrated that the mutual growth advantage of both cell types relies on contact-dependent mechanisms to ensure population stability.

One of the circuit features identified in this study is that proliferation of fibroblasts is limited by the carrying capacity of the environment. Carrying capacity can be defined by any environmental factor that limits population growth: for the same cell type this could be space, nutrients, or oxygen, depending on the tissue state. In our *in vitro* two-cell system, this limiting factor is likely the space available for cells to grow (Figure S4A). Similarly, proliferation of mammalian cells *in vivo* also can be limited by available space, as a function of total cell number, cell volume, and compartment size. The physical space, when defining carrying capacity, can be sensed, for example, through mechanosensory mechanisms of cell-cell or cell-matrix interactions (Humphrey et al., 2014). The Hippo signaling pathway that regulates contact-dependent growth inhibition (Yu et al., 2015) or mechano-sensitive GPCRs that control density-dependent proliferation (Gudipaty et al., 2017) are potential mechanisms determining carrying capacity *in vivo*. In addition, our results indicate that carrying capacity is tunable: increased growth factor availability can raise the carrying capacity of fibroblasts. As populations expand with enhanced growth factor signaling, space limitation intensifies the signal to suppress proliferation. The new carrying capacity is defined by the point at which both proliferative and anti-proliferative signals reach equilibrium. Such feedback mechanisms may allow tissue or organ size to scale with the level of growth signals. In this process, the balance between signals promoting and limiting growth is likely assessed and integrated to drive expression of genes controlling cell cycle progression. In tumors, oncogenic mutations that disrupt growth factor signaling pathways eliminate extrinsic growth limitation based on growth factor availability. Therefore, cancer cell growth becomes limited by oxygen and nutrients, rather than available growth factors (Ward and Thompson, 2012). The present experimental paradigm (Figures 4A and 4B) allows quantitative measurement of the carrying capacity of a cell type and dissection of the cellular mechanisms regulating cell proliferation and carrying capacity.

The other key circuit feature we observed is that circuit stability requires negative feedback to control the requisite growth factor for the cell type not limited by carrying capacity, in this case macrophages. This negative regulation is the "spring" in the "spring-and-ceiling" model (Figure 7G). Such feedback can occur through auto-repression or cross-repression, each generating different circuit topologies. In the present system, we find that auto-repression by receptor endocytosis-mediated growth factor depletion provides the required negative regulation. This internalization mechanism has been shown to have desirable features relative to cross-regulation (such as changes in growth factor production): internalization results in a circuit more robust to parameter variation that returns to stability more rapidly following perturbation (Adler et al., 2018).

A surprising finding from this study is that stability of macrophages and fibroblasts depends on cell-cell contact. This is

(D) Immunofluorescent images of MPs cultured with control or *Csf1* KO FBs after 7 days. Two representative fields of each condition are shown. FBs are transduced with lentivirus carrying GFP, and MPs are stained with anti-CD11b (red). Scale bar, 50 μm.

(E) Time-lapse imaging of interactions between MPs and FBs. TdTomato$^+$ FBs (red) and CSF1R-GFP (green) MPs were imaged 3 hr after plating. Arrows and arrowheads denote MPs. Arrows mark the daughter cells from a dividing MPs. Scale bar, 50 μm.

(F) Ratios between GFP$^+$ (control or *Csf1* KO) FBs and TdTomato$^+$ WT FBs in co-culture with MPs. 10,000 GFP$^+$ FBs and 10,000 TdTomato$^+$ FBs were combined and plated together with 40,000 MPs. (Data are representative of two independent experiments, n = 3.)

(G) Schematic of the "spring-and-ceiling" model of the MP-FB circuit. MPs and FBs maintain a stable circuit due to carrying capacity preventing FBs from expanding ("ceiling") and negative regulation controlling MP cell numbers relative to fibroblasts (arrows, "spring").

Data are represented as mean ± SD. See also Figure S6 and Movies S2 and S3.

reminiscent of the interactions between hematopoietic stem cells and their niche cells in the bone marrow (Cordeiro Gomes et al., 2016). Niche cells provide Notch and Wnt signals to maintain hematopoietic stem cells, as well as instructive signals for their differentiation (Reya and Clevers, 2005). Stem cells, in turn, produce signals such as PDGFB to modify niche cells (Damm and Clements, 2017). The number of stem cells is determined by the number of stem cell niches, which is likely limited by extrinsic factors (carrying capacity), such as available space. In addition, bone marrow niche cells express *Cxcl12*, which is a chemoattractant for *Cxcr4*-expressing hematopoietic stem cells (Cordeiro Gomes et al., 2016). Similarly, we observe high expression of *Cxcl12* in fibroblasts, which may attract *Cxcr4*-expressing macrophages to facilitate CSF1-dependent contact (Figure S6E). It is interesting to note that the CSF1-dependent association provides growth and survival benefits for both macrophages and fibroblasts. As a result, cells that consume but do not produce growth factors exhibit limited expansion. This mechanism may promote mutually beneficial ‘‘social’’ behaviors and ensure a reliable measurement of relative cell abundance. Further investigation will clarify the mechanisms underlying contact-dependent growth factor exchange between macrophages and fibroblasts.

The importance of cell-cell circuitry has long been studied in the context of development. Since Alan Turing’s seminal work proposing that two different ‘‘substances’’ interacting with each other are sufficient to generate biological patterns autonomously (Turing, 1952), several examples have shown the importance of feedback between different cell types during tissue development (Ben-Zvi et al., 2011; Kageyama et al., 2008; Sprinzak et al., 2010). These studies shed light on the mechanisms regulating various tissue-level properties, such as developmental scaling and spatial pattern generation (Kondo and Miura, 2010). Our work provides an example of how cell-cell circuitry can be employed to maintain tissue stability during homeostasis. While this study identifies sufficient conditions for two-cell circuit stability, it does not investigate all possible circuit topologies and forms of regulation that may exist in a stable circuit. For example, cell circuit topologies likely differ based on the ability of cells to proliferate and/or differentiate. The macrophage-fibroblast circuit consists of two cell types that are capable of proliferation in a differentiated state in response to their respective growth factors. This is in contrast to interactions involving post-mitotic cells, such as neurons, where growth factor signaling is required for survival but does not promote proliferation (Crowley et al., 1994; Johnson et al., 1980). In fact, interactions between neurons and microglia, or between peripheral nerves and macrophages may provide distinct examples of growth factor-dependent circuits, where neurons produce CSF1 (Guan et al., 2016; Muller et al., 2014) and macrophages produce members of the nerve growth factor family (Lavin et al., 2014). Furthermore, distinct topologies may exist for circuits involving cells that continuously differentiate from stem/progenitor cells. In murine olfactory epithelium, negative feedback from differentiated cells can regulate the probability of their progenitor cells to choose between self-renewal or differentiation, while maintaining stable progenitor cell numbers (Lo et al., 2009). In contrast, in the intestinal crypt, frequent and stochastic stem cell loss and replacement may add additional complexity to tissue level topologies (Krieger and Simons, 2015). Lastly, circuit characteristics may change if additional regulatory mechanisms, such as secreted negative regulators, are considered. Quantitative analyses of different types of cell circuits will be necessary to fully elucidate tissue homeostasis.

In this study, we identified multiple theoretically possible stable cell circuits. Macrophages and fibroblasts use one of these circuits; however, it is likely that at least some of the other stable circuit topologies are used by other cell combinations. Each circuit topology has different characteristics, and it will be important to define which circuits are used by which cell types. In addition, each of the circuits may have specific vulnerabilities to dysregulation. For example, the macrophage-fibroblast circuit studied here has a state in which fibroblasts no longer require growth factor produced by macrophages. In tissues, this feature could be responsible for altered ratios of fibroblasts to other cell types, as occurs in fibrosis, where tissue composition shifts to a pathological stable state characterized by over-representation of fibroblasts (Decker et al., 2017). It would be interesting to determine in future studies whether characteristic vulnerabilities of different cell circuits result in specific types of disruption of tissue homeostasis, leading to fibrotic, degenerative, and neoplastic disorders.

STAR★METHODS

Detailed methods are provided in the online version of this paper and include the following:

- KEY RESOURCES TABLE
- CONTACT FOR REAGENT AND RESOURCE SHARING
- EXPERIMETAL MODEL AND SUBJECT DETAILS
    - Mice
    - Primary cultures
- METHOD DETAILS
    - Macrophage-fibroblast co-culture
    - Flow cytometry for cell quantification
    - EdU (5-ethynyl-2′-deoxyuridine) assay
    - Proliferation assay
    - Plasmid purification
    - Viral transduction
    - CRISPR knockout in macrophages
    - Imaging quantification of cell number
    - Adjustment for cell number quantification
    - Immunofluorescence
    - Live cell imaging and trace analysis
    - Growth factor uptake assay
    - RNA sequencing and analysis
    - RNA isolation and qRT-PCR
    - Analytical screening of circuit topologies
    - Adjustment for cell density dependence
    - Model circuit parameters
    - Modeling cell circuit perturbations
- QUANTIFICATION AND STATISTICAL ANALYSES
- DATA AND SOFTWARE AVAILABILITY

SUPPLEMENTAL INFORMATION

Supplemental Information includes six figures, three tables, and three movies and can be found with this article online at https://doi.org/10.1016/j.cell.2018.01.015.

ACKNOWLEDGMENTS

Work in the R.M. lab was supported by the Blavatnik Family Foundation, the Else Kroner-Fresenius Foundation, the Scleroderma Research Foundation, a grant from Biogen, and the Howard Hughes Medical Institute (HHMI). X.Z. is supported by the Jane Coffin Childs Memorial Fund postdoctoral fellowship. R.A. Franklin is supported by the CRI Donald Gogel postdoctoral fellowship. J.B.J. is supported by an NIH MSTP T32 training grant (T32GM007205) and an NRSA NCI fellowship (1F30CA189926-01). W.B. is supported by a CRI Irvington postdoctoral fellowship. J.S. is supported by NIH (F31AI133855). R.A. Flavell is supported in part by the HHMI. U.A. is the incumbent of the Abisch-Frenkel chair. We want to thank all current and former members of the Medzhitov and Alon labs for discussions.

AUTHOR CONTRIBUTIONS

X.Z. and R.A. Franklin performed all the experiments. M.A. and U.A. performed the circuit modeling with help from A.M. J.B.J. conducted the initial studies. W.B., J.A.S., and R.A. Flavell contributed the CRISPR guide plasmid. X.Z., R.A. Franklin, M.A., U.A., and R.M. analyzed the data and wrote the paper.

DECLARATION OF INTERESTS

All authors declare no competing interests.

Received: June 30, 2017
Revised: November 6, 2017
Accepted: January 8, 2018
Published: February 1, 2018

REFERENCES

Adler, M., Mayo, A.E., Zhou, X., Franklin, R.A., Jacox, J.B., Medzhitov, R., and Alon, U. (2018). Endocytosis as a stabilizing mechanism for tissue homeostasis. Proc. Natl. Acad. Sci. USA. Published online. https://doi.org/10.1073/pnas.1714377.

Andrae, J., Gallini, R., and Betsholtz, C. (2008). Role of platelet-derived growth factors in physiology and medicine. Genes Dev. *22*, 1276–1312.

Ben-Zvi, D., Pyrowolakis, G., Barkai, N., and Shilo, B.Z. (2011). Expansion-repression mechanism for scaling the Dpp activation gradient in Drosophila wing imaginal discs. Curr. Biol. *21*, 1391–1396.

Bray, N.L., Pimentel, H., Melsted, P., and Pachter, L. (2016). Near-optimal probabilistic RNA-seq quantification. Nat. Biotechnol. *34*, 525–527.

Chitu, V., and Stanley, E.R. (2006). Colony-stimulating factor-1 in immunity and inflammation. Curr. Opin. Immunol. *18*, 39–48.

Citri, A., and Yarden, Y. (2006). EGF-ERBB signalling: towards the systems level. Nat. Rev. Mol. Cell Biol. *7*, 505–516.

Cordeiro Gomes, A., Hara, T., Lim, V.Y., Herndler-Brandstetter, D., Nevius, E., Sugiyama, T., Tani-Ichi, S., Schlenner, S., Richie, E., Rodewald, H.R., et al. (2016). Hematopoietic stem cell niches produce lineage-instructive signals to control multipotent progenitor differentiation. Immunity *45*, 1219–1231.

Crowley, C., Spencer, S.D., Nishimura, M.C., Chen, K.S., Pitts-Meek, S., Armanini, M.P., Ling, L.H., McMahon, S.B., Shelton, D.L., Levinson, A.D., et al. (1994). Mice lacking nerve growth factor display perinatal loss of sensory and sympathetic neurons yet develop basal forebrain cholinergic neurons. Cell *76*, 1001–1011.

Damm, E.W., and Clements, W.K. (2017). Pdgf signalling guides neural crest contribution to the haematopoietic stem cell specification niche. Nat. Cell Biol. *19*, 457–467.

Davies, L.C., Jenkins, S.J., Allen, J.E., and Taylor, P.R. (2013). Tissue-resident macrophages. Nat. Immunol. *14*, 986–995.

Decker, M., Martinez-Morentin, L., Wang, G., Lee, Y., Liu, Q., Leslie, J., and Ding, L. (2017). Leptin-receptor-expressing bone marrow stromal cells are myofibroblasts in primary myelofibrosis. Nat. Cell Biol. *19*, 677–688.

Doench, J.G., Fusi, N., Sullender, M., Hegde, M., Vaimberg, E.W., Donovan, K.F., Smith, I., Tothova, Z., Wilen, C., Orchard, R., et al. (2016). Optimized sgRNA design to maximize activity and minimize off-target effects of CRISPR-Cas9. Nat. Biotechnol. *34*, 184–191.

Goh, L.K., and Sorkin, A. (2013). Endocytosis of receptor tyrosine kinases. Cold Spring Harb. Perspect. Biol. *5*, a017459.

Gotelli, N.J. (2008). A Primer of Ecology, Fourth Edition (Sinauer Associates).

Guan, Z., Kuhn, J.A., Wang, X., Colquitt, B., Solorzano, C., Vaman, S., Guan, A.K., Evans-Reinsch, Z., Braz, J., Devor, M., et al. (2016). Injured sensory neuron-derived CSF1 induces microglial proliferation and DAP12-dependent pain. Nat. Neurosci. *19*, 94–101.

Gudipaty, S.A., Lindblom, J., Loftus, P.D., Redd, M.J., Edes, K., Davey, C.F., Krishnegowda, V., and Rosenblatt, J. (2017). Mechanical stretch triggers rapid epithelial cell division through Piezo1. Nature *543*, 118–121.

Guilliams, M., and Scott, C.L. (2017). Does niche competition determine the origin of tissue-resident macrophages? Nat. Rev. Immunol. *17*, 451–460.

Harris, S.E., MacDougall, M., Horn, D., Woodruff, K., Zimmer, S.N., Rebel, V.I., Fajardo, R., Feng, J.Q., Gluhak-Heinrich, J., Harris, M.A., and Abboud Werner, S. (2012). Meox2Cre-mediated disruption of CSF-1 leads to osteopetrosis and osteocyte defects. Bone *50*, 42–53.

Hart, Y., Antebi, Y.E., Mayo, A.E., Friedman, N., and Alon, U. (2012). Design principles of cell circuits with paradoxical components. Proc. Natl. Acad. Sci. USA *109*, 8346–8351.

Hart, Y., Reich-Zeliger, S., Antebi, Y.E., Zaretsky, I., Mayo, A.E., Alon, U., and Friedman, N. (2014). Paradoxical signaling by a secreted molecule leads to homeostasis of cell levels. Cell *158*, 1022–1032.

Hawley, R.G., Fong, A.Z., Burns, B.F., and Hawley, T.S. (1992). Transplantable myeloproliferative disease induced in mice by an interleukin 6 retrovirus. J. Exp. Med. *176*, 1149–1163.

Heldin, C.H., and Westermark, B. (1999). Mechanism of action and in vivo role of platelet-derived growth factor. Physiol. Rev. *79*, 1283–1316.

Humphrey, J.D., Dufresne, E.R., and Schwartz, M.A. (2014). Mechanotransduction and extracellular matrix homeostasis. Nat. Rev. Mol. Cell Biol. *15*, 802–812.

Ip, W.K.E., Hoshi, N., Shouval, D.S., Snapper, S., and Medzhitov, R. (2017). Anti-inflammatory effect of IL-10 mediated by metabolic reprogramming of macrophages. Science *356*, 513–519.

Johnson, E.M., Jr., Gorin, P.D., Brandeis, L.D., and Pearson, J. (1980). Dorsal root ganglion neurons are destroyed by exposure in utero to maternal antibody to nerve growth factor. Science *210*, 916–918.

Kageyama, R., Ohtsuka, T., Shimojo, H., and Imayoshi, I. (2008). Dynamic Notch signaling in neural progenitor cells and a revised view of lateral inhibition. Nat. Neurosci. *11*, 1247–1251.

Karin, O., and Alon, U. (2017). Biphasic response as a mechanism against mutant takeover in tissue homeostasis circuits. Mol. Syst. Biol. *13*, 933.

Karin, O., Swisa, A., Glaser, B., Dor, Y., and Alon, U. (2016). Dynamical compensation in physiological circuits. Mol. Syst. Biol. *12*, 886.

Kondo, S., and Miura, T. (2010). Reaction-diffusion model as a framework for understanding biological pattern formation. Science *329*, 1616–1620.

Krieger, T., and Simons, B.D. (2015). Dynamic stem cell heterogeneity. Development *142*, 1396–1406.

Lavin, Y., Winter, D., Blecher-Gonen, R., David, E., Keren-Shaul, H., Merad, M., Jung, S., and Amit, I. (2014). Tissue-resident macrophage enhancer landscapes are shaped by the local microenvironment. Cell *159*, 1312–1326.

Lo, W.C., Chou, C.S., Gokoffski, K.K., Wan, F.Y., Lander, A.D., Calof, A.L., and Nie, Q. (2009). Feedback regulation in multistage cell lineages. Math. Biosci. Eng. *6*, 59–82.

Majno, G., and Joris, I. (2004). Cells, Tissues, and Disease: Principles of General Pathology, Second Edition (Oxford University Press).

May, R.M. (1973). Qualitative stability in model ecosystems. Ecology *54*, 638–641.

Muller, P.A., Koscsó, B., Rajani, G.M., Stevanovic, K., Berres, M.L., Hashimoto, D., Mortha, A., Leboeuf, M., Li, X.M., Mucida, D., et al. (2014). Crosstalk between muscularis macrophages and enteric neurons regulates gastrointestinal motility. Cell *158*, 300–313.

Nathan, C., and Ding, A. (2010). Nonresolving inflammation. Cell *140*, 871–882.

Okabe, Y., and Medzhitov, R. (2016). Tissue biology perspective on macrophages. Nat. Immunol. *17*, 9–17.

Payne, S., and You, L. (2014). Engineered cell-cell communication and its applications. Adv. Biochem. Eng. Biotechnol. *146*, 97–121.

Raff, M.C. (1992). Social controls on cell survival and cell death. Nature *356*, 397–400.

Raff, M.C. (1996). Size control: the regulation of cell numbers in animal development. Cell *86*, 173–175.

Reya, T., and Clevers, H. (2005). Wnt signalling in stem cells and cancer. Nature *434*, 843–850.

Schindelin, J., Arganda-Carreras, I., Frise, E., Kaynig, V., Longair, M., Pietzsch, T., Preibisch, S., Rueden, C., Saalfeld, S., Schmid, B., et al. (2012). Fiji: an open-source platform for biological-image analysis. Nat. Methods *9*, 676–682.

Sprinzak, D., Lakhanpal, A., Lebon, L., Santat, L.A., Fontes, M.E., Anderson, G.A., Garcia-Ojalvo, J., and Elowitz, M.B. (2010). Cis-interactions between Notch and Delta generate mutually exclusive signalling states. Nature *465*, 86–90.

Tinevez, J.Y., Perry, N., Schindelin, J., Hoopes, G.M., Reynolds, G.D., Laplantine, E., Bednarek, S.Y., Shorte, S.L., and Eliceiri, K.W. (2017). TrackMate: an open and extensible platform for single-particle tracking. Methods *115*, 80–90.

Trapnell, B.C., and Whitsett, J.A. (2002). Gm-CSF regulates pulmonary surfactant homeostasis and alveolar macrophage-mediated innate host defense. Annu. Rev. Physiol. *64*, 775–802.

Turing, A.M. (1952). The chemical basis of morphogenesis. Philos. Trans. Royal Soc. B *237*, 37–72.

Ward, P.S., and Thompson, C.B. (2012). Metabolic reprogramming: a cancer hallmark even warburg did not anticipate. Cancer Cell *21*, 297–308.

Wiktor-Jedrzejczak, W., Bartocci, A., Ferrante, A.W., Jr., Ahmed-Ansari, A., Sell, K.W., Pollard, J.W., and Stanley, E.R. (1990). Total absence of colony-stimulating factor 1 in the macrophage-deficient osteopetrotic (op/op) mouse. Proc. Natl. Acad. Sci. USA *87*, 4828–4832.

Wynn, T.A. (2008). Cellular and molecular mechanisms of fibrosis. J. Pathol. *214*, 199–210.

Youk, H., and Lim, W.A. (2014). Secreting and sensing the same molecule allows cells to achieve versatile social behaviors. Science *343*, 1242782.

Yu, F.X., Zhao, B., and Guan, K.L. (2015). Hippo pathway in organ size control, tissue homeostasis, and cancer. Cell *163*, 811–828.

STAR★METHODS

KEY RESOURCES TABLE

REAGENT or RESOURCE	SOURCE	IDENTIFIER
Antibodies		
Anti-Mouse CD45	eBioscience	Clone# 30-F11; RRID:AB_1548790
Anti-Mouse CD11b	eBioscience	Clone# M1/70; RRID:AB_469900
Anti-Mouse F4/80	eBioscience	Clone# BM8; RRID:AB_469452
Anti-Mouse PDGFRA	eBioscience	Clone# APA5; RRID:AB_2573399
Anti-Mouse PDGFRB	eBioscience	Clone# APB5; RRID:AB_1548743
Anti-Mouse CSF1R	eBioscience	Clone# AFS98; RRID:AB_465807
Anti-Mouse CD16/CD32	eBioscience	Clone# 93; RRID:AB_467135
Anti-Rat IgG (H+L) Alexa Fluor 594	eBioscience	Cat# A-11007; RRID:AB_10561522
Chemicals, Peptides, and Recombinant Proteins		
Murine CSF1	Peprotech	Cat# 315-02
Murine PDGF-AA	Peprotech	Cat# 315-17
Murine PDGF-BB	Peprotech	Cat# 315-18
Human PDGF-CC	Peprotech	Cat# 100-00CC
Human HB-EGF	Peprotech	Cat# 100-47
Murine IGF-1	Peprotech	Cat# 250-19
Human IGF-2	Peprotech	Cat# 100-12
Human FGF-7	Peprotech	Cat# 100-19
Human PDGF-DD	R&D Systems	Cat# 1159-SB-025/CF
Fluorescein isothiocyanate-dextran, average mol wt 3000-5000	Sigma-Aldrich	FD4 SIGMA; CAS# 60842-46-8
DAPI	Sigma-Aldrich	D9542 SIGMA; CAS# 28718-90-3
Hoechst 33342	Life Technologies/ ThermoFisher	Cat# H1399; CAS# 23491-52-3
MMLV reverse transcriptase	Clontech	Cat# 639574
Critical Commercial Assays		
Click-It Plus EdU Flow Cytometry Assay kit	ThermoFisher	Cat# C10634
CyQUANT Direct Cell Proliferation Assay	ThermoFisher	Cat# C35011
NucleoBond® Xtra Midi Kit	Clonetch	Cat# 740410
Lipofectamine 2000 kit	ThermoFisher	Cat# 11668019
X-tremeGene 9 DNA Transfection reagent	Sigma Aldrich	Cat# 6365779001
123count eBeads	ThermoFisher	Cat# 01-1234-42
Mouse/Rat PDGF-BB Quantikine ELISA Kit	R&D Systems	Cat# MBB00
Mouse M-CSF Quantikine ELISA Kit	R&D Systems	Cat# MMC00
RNeasy kit	QIAGEN	Cat# 74106
Illumina TruSeq stranded mRNA preparation kits	Illumina	Cat# 20020594/20020595
PerfeCTa SYBR Green SuperMix	Quanta Biosciences	Cat# 95054
LIVE/DEAD fixable blue dead cell stain	ThermoFisher	Cat# L23105
ProLong Diamond Antifade Mountant	ThermoFisher	Cat# P36965
Deposited Data		
RNaseq data of macrophages and fibroblasts	This study	GSE104511
RNaseq data of tissue resident macrophages	Lavin et al., 2014	GSE63341
Experimental Models: Organisms/Strains		
Mouse: C57BL/6J	The Jackson Laboratory	JAX: 000664
Mouse: B6N.Cg-Tg(Csf1r-EGFP)1Hume/J	The Jackson Laboratory	JAX: 018549

(*Continued on next page*)

Continued

REAGENT or RESOURCE	SOURCE	IDENTIFIER
Mouse: B6.Cg-*Gt(ROSA)26Sor*$^{tm14(CAG\text{-}tdTomato)Hze}$/J	The Jackson Laboratory	JAX: 007914
Mouse: C57BL/6-Tg(CD68-EGFP)1Drg/J	The Jackson Laboratory	JAX: 026827
Mouse: C57BL/6-Tg(Pdgfra-cre)1Clc/J	The Jackson Laboratory	JAX: 013148
Mouse: B6(C)-*Gt(ROSA)26Sor*$^{em1.1(CAG\text{-}cas9^{*},\text{-}EGFP)Rsky}$/J	The Jackson Laboratory	JAX: 028555
Mouse: Csf1$^{fl/fl}$	Harris et al., 2012	N/A
Oligonucleotides		
DNA oligonucleotides used for expression analysis and CRISPR knockout, see Table S1	This study	N/A
Recombinant DNA		
Plasmid: pMSCVpuro-Cre/IRES-GFP	Ip et al., 2017	N/A
Plasmid: pMSCVpuro-IRES-GFP	Ip et al., 2017	N/A
Plasmid: pCL-Eco retrovirus packaging vector	Novus biologicals	CAT# NBP2-29540
Plasmid: MSCV-sgRNA (MGguide)	Gift from R. A. Flavell	N/A
Plasmid: MSCV-PDGFB-sgRNA	This study	N/A
Software and Algorithms		
Kallisto	Bray et al., 2016	https://pachterlab.github.io/kallisto/
Fiji / ImageJ	Schindelin et al., 2012	https://fiji.sc/
TrackMate v2.8.1	Tinevez et al., 2017	N/A

CONTACT FOR REAGENT AND RESOURCE SHARING

Further information and requests for resources and reagents should be directed to and will be fulfilled by the Lead Contact, Ruslan Medzhitov (ruslan.medzhitov@yale.edu).

EXPERIMETAL MODEL AND SUBJECT DETAILS

Mice

Male and female C57BL/6J (stock #000664), CSF1R-EGFP (stock #018549), Rosa26-TdTomato (stock #007914), CD68-EGFP (stock #026827), Pdgfra-cre (stock #013148), and Cas9 (stock #028555) mice (6 to 8 weeks old) were purchased from Jackson Laboratory. *Csf1*$^{fl/fl}$ mice were generously provided by Sherry Abboud-Werner (Harris et al., 2012). Mice were maintained in a specific pathogen-free facility and all animal experiments were performed in accordance with institutional regulations after protocol review and approval by Yale University's Institutional Animal Care and Use Committee.

Primary cultures

Bone marrow-derived macrophages

Bone marrow-derived macrophages (BMDMs) were differentiated from whole bone marrow from female mice (8 to 12 weeks old) in the presence of L929-conditioned media. Femurs and tibias were removed from mice, flushed, and exposed to hypotonic lysis (ACK lysing buffer, ThermoFisher) to remove red blood cells. Cells were plated in macrophage growth media (MGM) overnight (RPMI + 2 mM L-glutamine, 1 mM sodium pyruvate, 10 mM HEPES, 200 U/mL penicillin/streptomycin, 10% FBS, and 30% L929-conditioned media). The next day (day 1), nonadherent cells were harvested, washed, and replated in 15 cm Petri dishes in 20 mL of MGM. On day 4, 15 mL of MGM was added to the plate. On Day 6-7, cells were lifted with 3 mM cold EDTA in PBS for 15 min and plated at appropriate concentrations for coculturing. All cell cultures were maintained in a 37°C incubator at 5% CO_2.

Mouse embryonic fibroblasts

Mouse embryonic fibroblasts (MEFs) were harvested from male and female E13.5-E14.5 embryos and sorted for purity. Staged embryos were removed from a pregnant female by removing the uterus and separating each embryo from its amniotic sac. The head and "red tissue," including fetal liver, were removed and discarded. If genotyping was required, the head served as the source of DNA and embryos were kept separated. The remaining portion of each embryo was minced using razor blades in 0.05% trypsin + EDTA and placed in a 37°C incubator for 30 min. After digestion, the tissue was transferred into a conical tube, washed with complete DMEM (DMEM + 2 mM L-glutamine, 1 mM sodium pyruvate, 10 mM HEPES, 200 U/mL penicillin/streptomycin, 10% FBS; GIBCO) and resuspended in complete DMEM in 15 cm tissue culture plates overnight. The following day, cells and undigested tissue debris were lifted from the plates using 0.05% trypsin + EDTA, spun down, resuspended, and filtered over a 70 μm filter. These cells were expanded for 1-2 passages and then sorted for CD45-, CD11b-, and F4/80-negativity to exclude contaminating macrophages. The sorted MEFs were split once after sorting to allow for recovery and used for experiments at p4-p7.

METHOD DETAILS

Macrophage-fibroblast co-culture

All co-cultures were plated in a 1:1 ratio of complete DMEM to complete RPMI with 2% FBS (co-culture media, CCM) in 6-well tissue culture treated plates (Falcon). Day 6-7 BMDMs and p4-p7 MEFs were plated together without any additional supplementation of growth factors in 6-well tissue culture plates, unless noted. For long-term co-culture, the media was replenished every 2-3 days for the duration of the experiment by removing 200 μL of media, and adding 400 μL of fresh CCM. The total media volume remained relatively constant throughout the experiment.

Flow cytometry for cell quantification

MEFs and BMDMs were harvested from tissue culture plates first by incubation with 0.05% Trypsin + EDTA, and next by cell scraping to remove any remaining attached cells. Cells were washed and transferred to round-bottom 96-well plates for FACS staining. Fluorochrome-conjugated antibodies against CD45 (clone 30-F11), CD11b (M1/70), F4/80 (BM8), PDGFRA (APA5), PDGFRB (APB5), and CSF1R (AFS98) were purchased from eBioscience/ThermoFisher. Dead cells were excluded using ThermoFisher LIVE/DEAD Fixable Blue Dead Cell Stain and binding to Fc receptors was blocked using CD16/CD32 (clone 93, eBioscience/ThermoFisher). All samples were acquired on a Becton Dickinson LSR II Flow cytometer and analyzed using FlowJo.

EdU (5-ethynyl-2′-deoxyuridine) assay

Mono-cultures or co-cultures were plated in 6-well tissue culture plates 1-11 days prior to EdU incorporation assay, depending on the experiment. EdU (10 μM) was added to the cells for 2 hr and the cells were harvested as above. Cells were first stained with surface antibodies and then EdU incorporation was detected using the Click-iT Plus EdU Flow Cytometry Assay Kit according to the manufacturer’s instructions (ThermoFisher). Samples were then acquired on a Becton Dickinson LSR II Flow cytometer and analyzed using FlowJo.

Proliferation assay

MEFs or BMDMs were plated in 96-well tissue culture treated plates in complete DMEM or complete RPMI, respectively. Beginning 4-6 hr after plating, growth factors were added once daily for the duration of the experiment. To measure proliferation, live cells in each well were stained using CyQUANT Direct Cell Proliferation Assay (ThermoFisher) according to the manufacturer’s instructions. Absolute cell number was determined by plating known cell numbers and measuring fluorescent intensity to generate a standard curve. To improve reproducibility, standard curves determined with known cell numbers were calibrated with known concentrations of FITC-dextran beads (Sigma-Aldrich, FD4). FITC-dextran standard curves were used to calculate cell numbers daily.

Plasmid purification

All DNA vectors were transformed into *E. coli* (DH5a). Plasmids were purified with NucleoBond® Xtra Midi kit (Clonetch). The concentration and quality of plasmids were assessed with Nanodrop 8000 (ThermoFisher).

Viral transduction

Expression vectors pMSCVpuro-Cre/IRES-GFP (Cre-GFP) or pMSCVpuro-IRES-GFP (GFP) (Ip et al., 2017) were co-transfected into 293T cells with retrovirus packaging vector pCL-Eco using the Lipofectamine 2000 kit (ThermoFisher, #11668019) according to the manufacturer’s instructions. 24 hr after co-transfection, cell culture medium was changed to complete DMEM. After 24 hr, viral supernatant was collected, filtered through 0.45 μm filters and directly applied to low-passage unsorted MEFs through spin-fection at 1,300 x g for 2 hr at room temperature. Successfully transduced MEFs were sorted based on DAPI-negativity (100 ng/mL, Sigma Aldrich), CD45-negativity, and GFP-positivity, and allowed to rest for at least one passage before performing co-culture experiments.

CRISPR knockout in macrophages

The retroviral sgRNA vector (a gift from R.A. Flavell) was constructed using a Murine Stem Cell Virus (MSCV) backbone (Hawley et al., 1992) and subcloning a human U6 promoter driving a sgRNA cassette and an Sv40 promoter driving the expression of GFP. The guide RNA sequence for *Pdgfb* (Table S1) (Doench et al., 2016) was cloned into BbsI sites of the vector. On day 1, vectors expressing CRISPR guide RNA were co-transfected into 293T cells with retrovirus packaging vector Pcl-Eco using X-tremeGENE 9 DNA Transfection Reagent (Sigma Aldrich, #6365779001) according to the manufacturer’s instructions. On day 2, cell culture medium was changed to complete DMEM to collect viral particles. On the same day, bone marrow cells were isolated from Cas9-knock-in mice and plated in 12-well Petri dish plates in 1ml MGM at 1-2 million cells per well. On day 3, viral supernatant was collected and filtered through 0.45 μm filters. The filtered viral supernatant was added onto bone marrow cells at 1ml per well, with the addition of 50 ng/ml recombinant CSF1. On day 8, the transduced bone marrow macrophages were lifted with EDTA and sorted for GFP^{+} cells.

Imaging quantification of cell number

On day 0, TdTomato$^+$ MEFs (Pdgfra-cre x Rosa26-TdTomato mice) and GFP$^+$ BMDMs (CSF1R-EGFP mice) were plated in 6-well tissue culture treated plates in CCM. Cells were imaged on day 1 and day 3, or on day 2 and day 4. Hoechst 33342 (Life Technologies, H1399) was added to the media (1 μg/mL) to stain cell nuclei 30 min before imaging. Cell supernatant was removed and cells were gently washed once with warm PBS. Cells were then kept in PBS throughout the imaging process. 20 imaging fields were chosen to allow even coverage across the space of the well. For each imaging field, focal plane was established based on the intensity of nuclear staining (Hoechst) and 5 stacked images (every 5 μm) were taken around the focal plane to capture the peak intensity of the cellular fluorescence. GFP, RFP and DAPI channels were taken for every position. Duplicate wells were prepared for each cell density condition to reduce biological variation. Imaging was performed with Leica AF6000 Modular System (Leica) with stage-top incubator INUBTFP-WSKM-F1 (Tokai Hit) maintained at 37°C and 5% CO_2 to ensure optimal cell viability throughout the imaging process.

First, the maximum intensity projection was applied for all channels of each imaging field. Nuclear segmentation was performed with the DAPI image to identify cell location. Since noticeable differences in nuclear staining were observed between MEFs and BMDMs, gradient thresholding on nuclear staining was applied to ensure accurate identification of both cell types. Briefly, each image was first subtracted from its background with disk-smoothing method (‘strel’ option) and smoothed with a Gaussian filter for threshold segmentation. For each round of thresholding, the number, location, size, and intensity of cell nuclei were identified and recorded. As the threshold decreased gradually each round, the newly identified cell nuclei were compared with the ones identified in the previous round and only new cells were recorded. During this gradient segmentation, a sudden increase in new cells indicated background noise and therefore further segmentation was halted. The initial threshold (highest threshold) was set as the higher number between the default function setting (graythresh) and twice the background ratio. The background ratio was calculated as median intensity / maximum intensity for each image. The gradient of thresholds decreases in 10 evenly-spaced steps from the initial threshold to the background ratios. After gradient thresholding, the nuclear intensity of GFP and RFP channels were calculated.

Each image field was processed independently. Of all 20 image fields from the same well, the outliers were identified as the total cell numbers in an image that deviated more than 2 standard deviations from the average, and were removed from further analysis. For each identified nucleus, the cell type was determined in a sequence as follows.

i) the nucleus is removed from the analysis if any of the following is true: nuclei size < 30 pixels or > 2000 pixels (small or large particle contamination), or average DAPI signal < 5 or > 500 (contamination or dead cells), or average GFP signal < 2 and average RFP signal < 5 (unidentifiable cells).
ii) if RFP signal is over a high RFP threshold (> 100), the cell is a fibroblast.
iii) if the cell nucleus is small (size < 200 pixels) and with high intensity (> 30), the cell is a macrophage; if the nucleus is large (size > 200 pixels) and with lower intensity (< 30), it is a fibroblast.
iv) if GFP signal is over a threshold (> 4), it is a macrophage.
v) The remaining unidentified cells were further analyzed based on RFP signals and nuclei size (smaller nuclei (< 200) and low RFP signal (< 30) is a macrophage).

The thresholds were chosen empirically based on the distribution of the measurements and further fine-tuned based on specificity of sampled images. They are generally consistent across all datasets. The false discovery rate estimated based on fibroblast only images is less than 5%. Total cell number per well was calculated as the average cell density of all analyzed images. All images are 8-bit images with measurement value range from 0-255.

Adjustment for cell number quantification

Imaging quantification of cell numbers 12 hr after plating was highly consistent with the expected number (see above). However, harvesting of cultured cells for flow cytometry results in cell loss during sample preparation and analysis. In order to obtain accurate cell numbers while correcting for cell loss, counting beads (123count eBeads, Affymetrix) were added following harvest, immediately prior to running samples on the flow cytometer (50 μL of beads were added to 150 μL sample). Absolute cell numbers were calculated according to manufacturer’s instructions, using the following equation: ((# of live single cells acquired * 0.05)/(# of beads acquired * 0.15)) * eBead concentration. To correct for cell loss, we applied a standard curve adjustment based on the original cell number plated and the bead-calculated cell number. Cell numbers generated from imaging quantification and flow cytometry after this adjustment were consistent.

Immunofluorescence

Cells were cultured in 8-well chamber slides, fixed in 4% paraformaldehyde and permeabilized using 0.1% saponin in blocking buffer (HBSS containing 3% BSA, 0.2% gelatin, and 0.02% NaN_3) and stained with Rat anti-mouse CD11b (eBioscience, clone M1/70) and Goat anti-rat IgG (H+L) Alexa Fluor 594 secondary (ThermoFisher, A-11007). Hoechst 33342 was used to stain nuclei. Cells were mounted on microscope slides with ProLong Diamond Antifade Mountant (Molecular Probes). MEFs transduced with GFP or Cre-GFP were directly visualized. Imaging was performed with Leica AF6000 Modular System (Leica).

Live cell imaging and trace analysis

TdTomato$^+$ MEFs and CSF1R-EGFP BMDMs were plated in 6-well tissue culture treated plates in CCM. Image acquisition typically began 4-6 hr after plating cells using a Leica AF6000 Modular System (Leica) with stage-top incubator INUBTFP-WSKM-F1 (Tokai Hit) maintained at 37°C and 5% CO$_2$. Images were acquired every 10 mins for approximately 16 hr. The processing of image data was performed with ImageJ (Schindelin et al., 2012).

Trace analysis of cell movement was analyzed with cell tracking plug-in tool TrackMate v2.8.1 (Plugins- > tracking- > TrackMate) in ImageJ (Tinevez et al., 2017). The GFP (macrophage) and RFP (fibroblast) channels were processed independently with TrackMate for each dataset. "LoG detector" (Laplacian of Gaussian) is applied to filter image, with estimated blob diameter set to 0.2-0.25 and a threshold of 0.05-0.1 adjusted to each dataset. After the initial identification, cell spots on the edge of the image were removed from each image in the series. Then cell spots were selected by adjusting the threshold of signal/noise ratio for optimal specificity and accuracy. After cell identification, the information of assigned cell ID, cell position in every image, and time were extracted for downstream analysis in MATLAB. First, for each cell ID, any time gap in the identified trace was filled by assuming linear movement of the cell. Second, the movement velocity at every time point was calculated based on the position of the cells at the adjacent two time points. The velocity of macrophages was then analyzed with respect to its distance to the nearest fibroblast. Overall, 10 independent time series were analyzed.

Growth factor uptake assay

50,000 MEFs and 500,000 BMDMs were plated in 12-well plates in CCM overnight without exogenous growth factors. The next day, PDGFB (10 ng/mL) was added to wells containing MEFs, and CSF1 (10 ng/mL) was added to wells containing BMDMs. 20 uL samples of supernatant were taken from each well beginning immediately after growth factor was added (time 0) and at each subsequent time point (15 min, 30 min, 1 hr, 2 hr, 4 hr, 6 hr, 8 hr, 24 hr, 48 hr). Samples were frozen immediately on dry ice and thawed together for quantification by ELISA using the Mouse/Rat PDGF-BB Quantikine ELISA Kit (R&D Systems, MBB00) and Mouse M-CSF Quantikine ELISA Kit (R&D Systems, MMC00) according to the manufacturer's instructions. Plates were read using the SpectraMax M5 plate reader (Molecular Devices).

RNA sequencing and analysis

Day 6 WT BMDMs were plated in 12-well tissue treated plates at 750,000/well in MGM. Primary WT MEFs were plated in 6-well tissue treated plates at 100,000/well in complete DMEM. After overnight culture, adherent cells were washed twice with ice-cold PBS and collected with RLT buffer (QIAGEN RNeasy kit). RNA was purified from cells using QIAGEN RNeasy columns with on-column DNase digestion according to the manufacturer's instructions. Sequencing libraries were constructed following Illumina Tru-seq stranded mRNA protocol. Paired-end sequencing was performed with Next-seq 500 with 76 bp reads from each end.

Illumina fastq files were downloaded from Illumina Basespace and were aligned with Kallisto program with default settings (Bray et al., 2016) against all cDNA transcripts in mouse genome annotation GRCm38 (ftp://ftp.ensembl.org/pub/release-90/fasta/mus_musculus/cdna/s). The ENSEMBL IDs of each cDNA transcript were matched to the official gene symbols through BioaRt in R. The expression of each transcript is expressed in TPM (transcript per million). When multiple transcripts match to the same gene, the expression of the gene is calculated by summing the TPM of all matched transcripts.

RNA isolation and qRT-PCR

RNA was purified from cells using QIAGEN RNeasy columns according to the manufacturer's instructions. cDNA was reverse-transcribed with MMLV reverse transcriptase (Clontech) using oligo-dT$_6$ primers. qRT-PCR was performed on a CFX96 Real-Time System (Bio-Rad) using PerfeCTa SYBR Green SuperMix (Quanta Biosciences). Relative expression units were calculated as transcript levels of target genes relative to *Hprt1* or *Rpl13a* *1000. Primers used for qRT-PCR are listed in Table S1.

Analytical screening of circuit topologies

The analytical screening and model for the two-cell circuits are fully described in Adler et al. (2018). We model the concentrations of the cells (X_i) and growth factors (C_{ij}) by considering terms for proliferation/production and removal:

$$\dot{X}_1 = X_1\left(\lambda_1 h(C_{21})\left(1 - \frac{X_1}{K}\right) - \mu_1\right) \tag{1}$$

$$\dot{X}_2 = X_2(\lambda_2 h(C_{12}) - \mu_2) \tag{2}$$

$$\dot{C}_{12} = \beta_{12}X_1\left(1 - \frac{1}{2}\theta(1+\theta) + \theta h(C_{21})\right) + \beta_{22}X_2 - \alpha_{12}X_2 h(C_{12}) - \gamma C_{12} \tag{3}$$

$$\dot{C}_{21} = \beta_{21} X_2 \left(1 - \frac{1}{2}\omega(1+\omega) + \omega h(C_{12}) \right) + \beta_{11} X_1 - \alpha_{21} X_1 h(C_{21}) - \gamma C_{21} \tag{4}$$

In the equations for the cells (Equations 1 and 2), λ_i and μ_i are the maximal proliferation rate and removal rate of cell type *i*, respectively. The proliferation terms are multiplied by a Michaelis-Menten function, $h(C_{ij}) = C_{ij}/(k_{ij} + C_{ij})$, that describes binding of the growth factor to its cognate receptor on the target cell with halfway-effect at k_{ij}. Here, X_1 is assumed to be close to carrying capacity, *K*, whereas X_2 is assumed to be far from its carrying capacity.

The equations for the growth factors (Equations 3 and 4) have two terms of production with a paracrine signaling maximal secretion rate (β_{ij}), and an autocrine signaling secretion rate (β_{jj}). The numbers θ and ω describe the cross-regulation effect between the growth factors with $\theta, \omega = -1$ for downregulation, $\theta, \omega = 1$ for upregulation, and $\theta, \omega = 0$ for no interaction.

The removal terms in Equations 3 and 4 describe removal of growth factors through endocytosis with maximal internalization rate of α_{ij}, and a linear degradation term with rate γ.

Considering the different values for $\theta,\ \omega$, and substituting zero or non-zero values in the autocrine (β_{ii}) and endocytosis (α_{ij}) rates, results in the equations for all 144 possible circuit topologies.

Adjustment for cell density dependence

Cell-density dependence was introduced by considering the probability of a macrophage and a fibroblast forming an interaction. The number of cells within a given distance follows a Poisson distribution assuming cells are uniformly scattered. We therefore assume that the probability of two cells interacting follows a Poisson distribution: $p(\lambda) = 1 - e^{-\lambda}$, where $\lambda = X_1 X_2 / \sigma^2$ is the average number of interacting cells in a cross section σ (sigma is in units of number of cells per well, given that X_1 and X_2 are cells/well). The cross section σ that best fits the experimental data is $\sigma = 10^5$ cells per well (see next section for fitting method).

We plotted the corrected phase portrait by using rescaled axes $(\tilde{X}_1,\ \tilde{X}_2)$ equal to the number of cells $(X_1,\ X_2)$ multiplied by the probability of an interaction between the two cell types, $p(\lambda)$:

$$\tilde{X}_1 = \left(1 - e^{-\frac{X_1\ X_2}{\sigma^2}} \right) X_1 \tag{5}$$

$$\tilde{X}_2 = \left(1 - e^{-\frac{X_1\ X_2}{\sigma^2}} \right) X_2 \tag{6}$$

Since this rescaling is a post-processing step, it did not enter into the dynamics of the equations (and hence did not affect features such as fixed point stability), but only deformed the phase portrait at low density regions (density < $\sim$sigma).

Model circuit parameters

The model has 13 parameters (Equations 1, 2, 3, and 4 with $\beta_{22} = 0$). Instead of fitting these parameters to the stream plot, which may result in over-fitting, we chose to use a biologically plausible parameter set. For 5 of the parameters, we used the values that are approximated from experimental measurements: proliferation rates, $\lambda_1 = 0.9/day$, $\lambda_2 = 0.8/day$, death rates, $\mu_1 = 0.3/day$, $\mu_2 = 0.3/day$, and carrying capacity $K = 10^6 cells$. We used a low degradation rate for the growth factors, $\gamma = 0.08/hour$. For the remaining 7 parameters, we used values in the range of the values reported in the literature (Bionumbers database, http://bionumbers.hms.harvard.edu/), and adjusted them within their range to visually agree with the stream plot. These values are: secretion rates of growth factors, $\beta_{11} = 2.4x10^2 (molecules/cell\ min)$, $\beta_{12} = 4.7x10^2 (molecules/cell\ min)$, $\beta_{21} = 0.7x10^2 (molecules/cell\ min)$ (range $= 10 - 10^3 (molecules/cell\ min)$, BNID 112718), internalization rates of growth factors, $\alpha_{12} = 9.4x10^2 (molecules/cell\ min)$, $\alpha_{21} = 5.1x10^2 (molecules/cell\ min)$ (range $= 10^2 - 10^3 (molecules/cell\ min)$, BNID 112725), binding affinities Kd's of growth factors, $k_{12} = 1.8x10^7 molecules = 1.8x10^{-2} nM$, $k_{21} = 2.3x10^7 molecules = 2.3x10^{-2} nM$, for a well of 9.5 cm^2 surface area (range $10^{-2} - 10^{-1}$ nM, https://www.rndsystems.com/) (Table S2). We assumed an effective volume of $10^9\ \mu m^3$, which corresponds to growth factor in a 1 μm layer above the cells in a well of area 9.5 cm^2.

To determine whether the model stream plot is comparable to the experimental stream plot within experimental errors, we first estimated the error distribution of cell concentration measurements in day-day experimental repeats, $P(e)$, where $e = \log_{10}(repeat1/repeat2)$. This distribution is long tailed, and resembles a student-t distribution with parameters $\mu = -6x10^{-3}$, $\sigma = 0.1$, $\vartheta = 2.5$. Next, we computed the residuals of the model compared to the data: for each of the arrow-heads in the stream plot we calculated the deviation of model from the measurement $r_i = \log_{10}(model_i/experiment_i)$, with $i = 1, \ldots, N$ where $N = 108$ is the number of measurements (54 concentrations of FB and MP). We find that the residual distribution is centered at zero and has a width $std = 0.23$ that is consistent with the experimental error $std = 0.16$. We conclude that the model with the biologically plausible parameter set matches the experiment within experimental error (Figure S5E).

Next, we tested the effect of varying the parameters on the stream plot. We varied each of the model parameters described above (Table S2) by 20% and calculated the new fixed points. All parameters can be varied by 20%, and still keep the positons of the fixed points to within 48% of the reference parameter set (Table S3). The secretion, internalization, proliferation and death rates parameters primarily affect the ‘ON’ state fixed point position and not the separatrix, whereas the binding affinities and the degradation rates of the growth factors affect the separatrix position and not the fixed points. Varying both secretion and internalization rates as well as varying both proliferation and death rates while keeping their ratio constant $((\beta_{12}/\alpha_{12}),\ (\beta_{21}/\alpha_{21}),(\lambda_1/\mu_1),(\lambda_2/\mu_2))$ have small effect on the position of the fixed points.

To determine the density-correction parameter σ, we calculated the unstable point (X_{1u}, X_{2u}) of the phase portrait (Figure 5E). For this purpose, we set Equations 1, 2, 3, and 4 to zero, and solved them numerically with the parameter set described above. We identified the unstable point by calculating the eigenvalues of the Jacobian of the system. The resulted unstable point is described by fibroblasts number since $X_{2u} = 0$. We find σ by solving for the density -corrected value $(\tilde{X}_{1u})$, the following equation: $X_{1u} = (1 - e^{-(\tilde{X}_{1u}^2/\sigma^2)})\tilde{X}_{1u}$.

Modeling cell circuit perturbations

In order to model the experiments of Figure 6A, we used the same biologically plausible parameters from the phase portrait in Figure 5C (Table S2) except for $\beta_{11} = 1.6x10^2(molecules/cell\ min)$, let the system reach steady state, and then perturbed the concentration of a given cell type or growth factors. We used the function ParametricNDSolveValue in Mathematica 10.4 in order to solve the dynamics.

QUANTIFICATION AND STATISTICAL ANALYSES

We used unpaired t tests to determine statistical significance between groups ($p < 0.05$ was considered significantly different) using Prism. The specific statistical parameters are represented in the Figure Legend of each Figure. All data points are presented as Mean ± SD, unless specified. *$p < 0.05$; ** $p < 0.005$; *** $p < 0.0005$; **** $p < 0.00005$. In the Figure Legends, “n” represents the number of samples per condition from 1 independent experiment, unless specified.

DATA AND SOFTWARE AVAILABILITY

The accession number for the RNA sequencing data reported in this paper is GEO: GSE104511. Customized scripts for imaging analysis in MATLAB and circuit modeling in Mathematica are available upon reasonable request.

Supplemental Figures

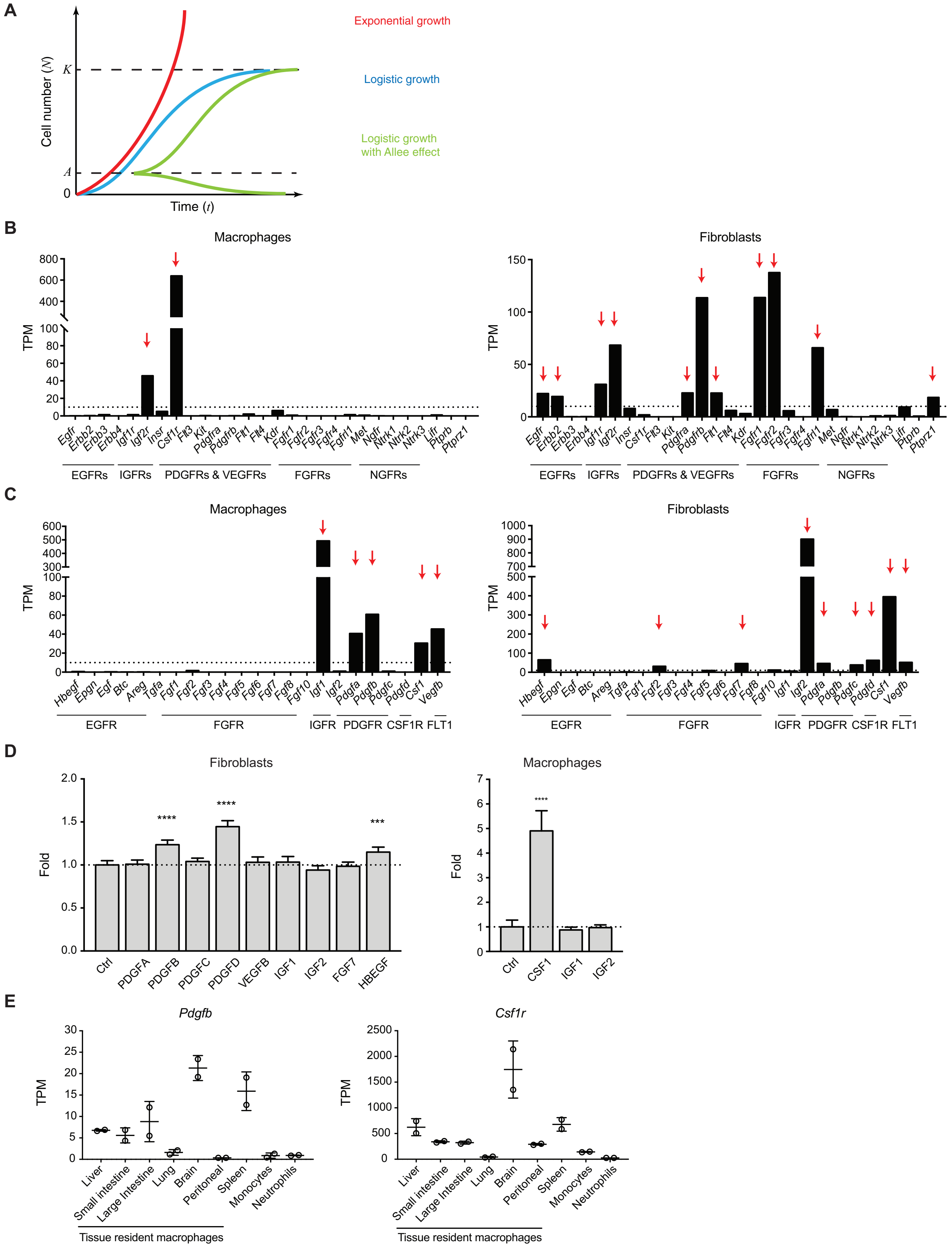

(legend on next page)

Figure S1. Macrophages and Fibroblasts Express Specific Growth Factors and Their Receptors, Related to Figure 1

(A) Schematic showing three different patterns of population growth. K, carrying capacity; A, Allee number; β, proliferation rate.

(B) Expression of growth factor receptors (receptor tyrosine kinase genes) in MP and FB as measured by RNA-seq. A threshold of 10 TPM (Transcripts Per Million) (dotted line) is used to identify receptors with high expression (marked with red arrows).

(C) Expression of growth factors that bind to the highly-expressed growth factor receptors in (A) as measured by RNA-seq. A threshold of 10 TPM (dotted line) is used to identify growth factors with high expression (marked with red arrows). Growth factors are grouped based on receptor usage.

(D) Screening of candidate growth factors for promoting proliferation of FB and MP. Cells were cultured in medium supplemented with 10% FBS and fed with growth factors daily for 4 days (50 ng/ml). Cell numbers were normalized to FB or MP numbers without the addition of growth factors (Ctrl). ***$p < 0.0005$, ****$p < 0.00005$, Student’s t test (data representative of two independent experiments, n = 7).

(E) Expression of *Pdgfb* and *Csf1r* in tissue-resident macrophages (Lavin et al., 2014).

Data are represented as Mean ± SD.

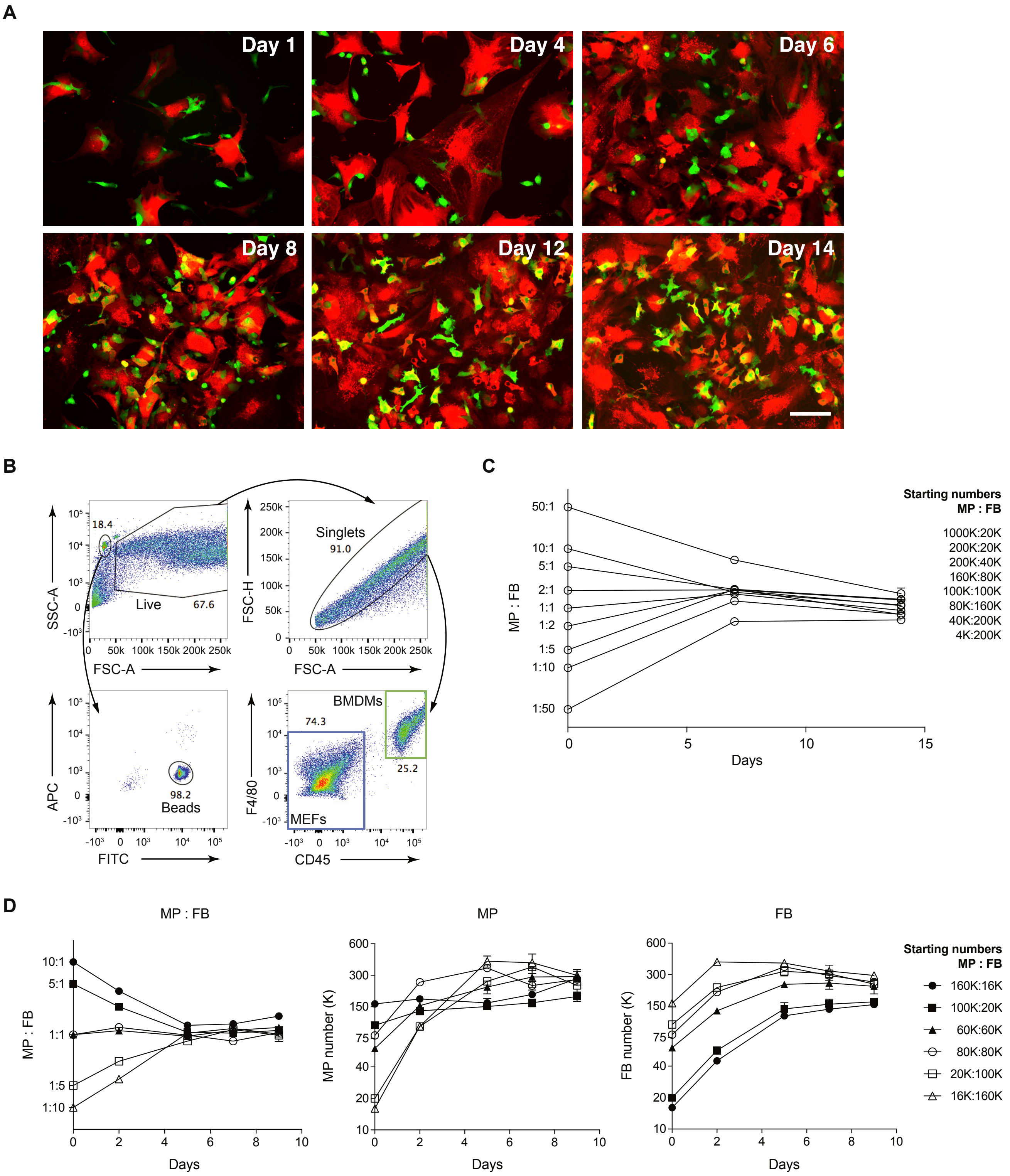

Figure S2. Macrophages and Fibroblasts Reach Stable Cell Numbers and Population Ratios, Related to Figure 2

(A) Representative fluorescent images of MP and FB co-cultures over time. MP were harvested from CD68-EGFP mice (green) and FB from Pdgfra-cre-Rosa26-TdTomato mice (red). Scale bar indicates 100 μm.

(legend continued on next page)

(B) Representative gating strategy for MP and FB in co-culture experiments. Cells were gated by forward and side scatter, singlets, and co-expression of CD45 and F4/80 (BMDMs, MP) or lack of CD45 and F4/80 expression (MEFs, FB). Counting beads were gated by forward and side scatter and FITC fluorescence. Absolute cell numbers were calculated using counting beads, and then corrected for cell loss during harvest (see the STAR Methods).

(C) Time course of population ratios for co-cultured MP and FB with starting ratios of 50:1 (1,000,000 & 20,000), 10:1 (200,000 & 20,000), 5:1 (200,000 & 40,000), 2:1 (160,000 & 80,000), 1:1 (100,000 & 100,000), 1:2 (80,000 & 160,000), 1:5 (40,000 & 200,000), 1:10 (20,000 & 200,000), and 1:50 (4,000 & 200,000) (data representative of more than five independent experiments, n = 3).

(D) Time course of co-cultured MP and FB with starting ratios of 10:1 (160,000 & 16,000), 5:1 (100,000 & 20,000), 1:1 (80,000 & 80,000 and 60,000 & 60,000), 1:5 (20,000 & 100,000), and 1:10 (16,000 & 160,000). MP:FB ratio, MP number, and FB number are shown (data representative of more than five independent experiments, n = 2).

Data are represented as Mean ± SD.

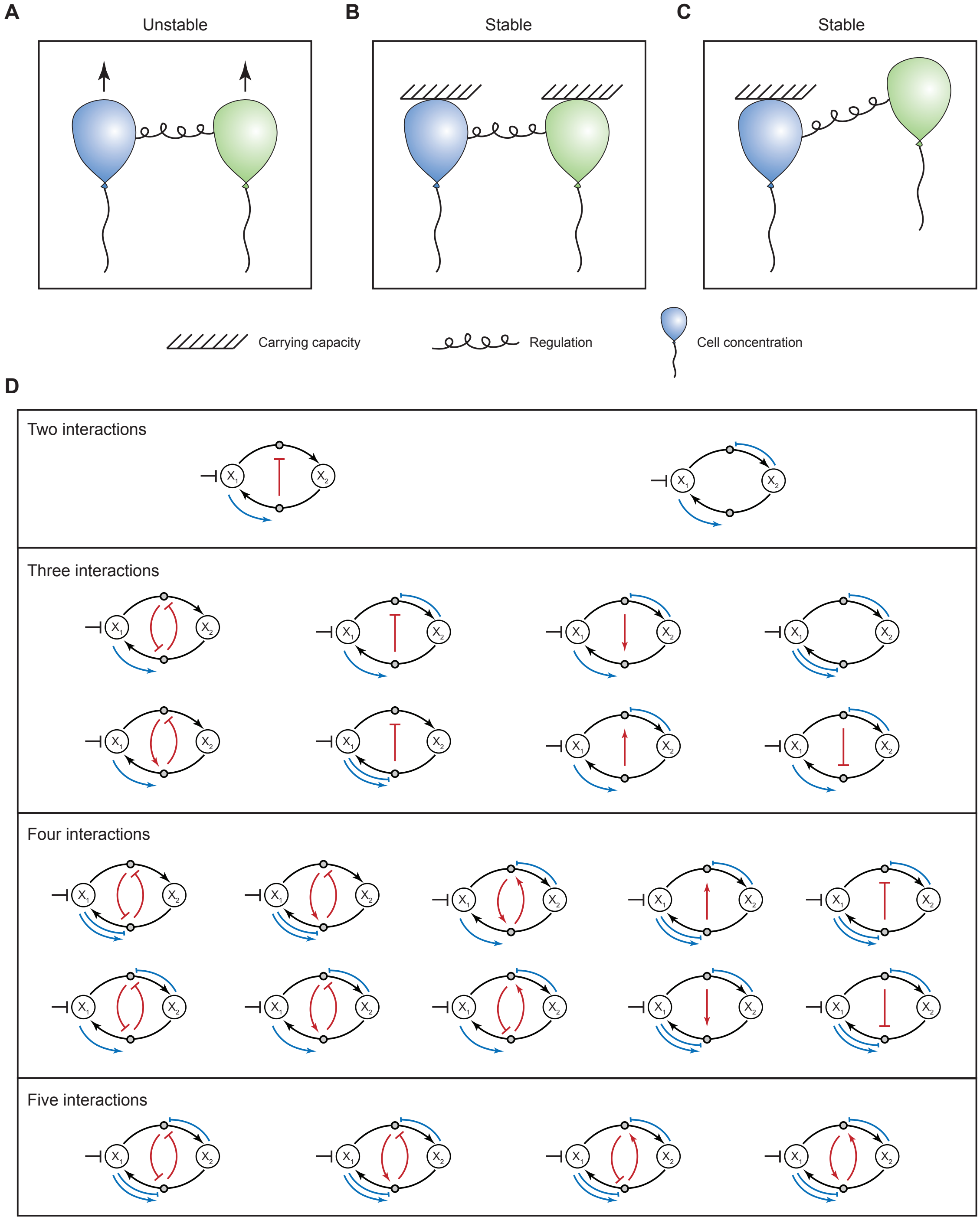

Figure S3. Analytical Screening Identifies All Stable Two-Cell Circuits, Related to Figure 3

(A–C) Schematic depicting possible interactions between two different cell types. The first situation is unstable because neither cell type is close to carrying capacity and therefore no amount of regulation will result in a stable 'ON' state (A). The second situation, when both cell types are close to carrying capacity, is stable and no additional regulation is required because the carrying capacities enforce an 'ON' state (B). The last situation, where one cell type is close to carrying capacity and the other is not, requires that the growth factor of the cell far from carrying capacity undergoes negative regulation in order to achieve a stable 'ON' state (C).

(D) Hierarchical representation of the 24 stable circuits that possess all three stable states, 'OFF,' 'ON,' and 'ON-OFF.' Circuits are grouped based on the total number of interactions.

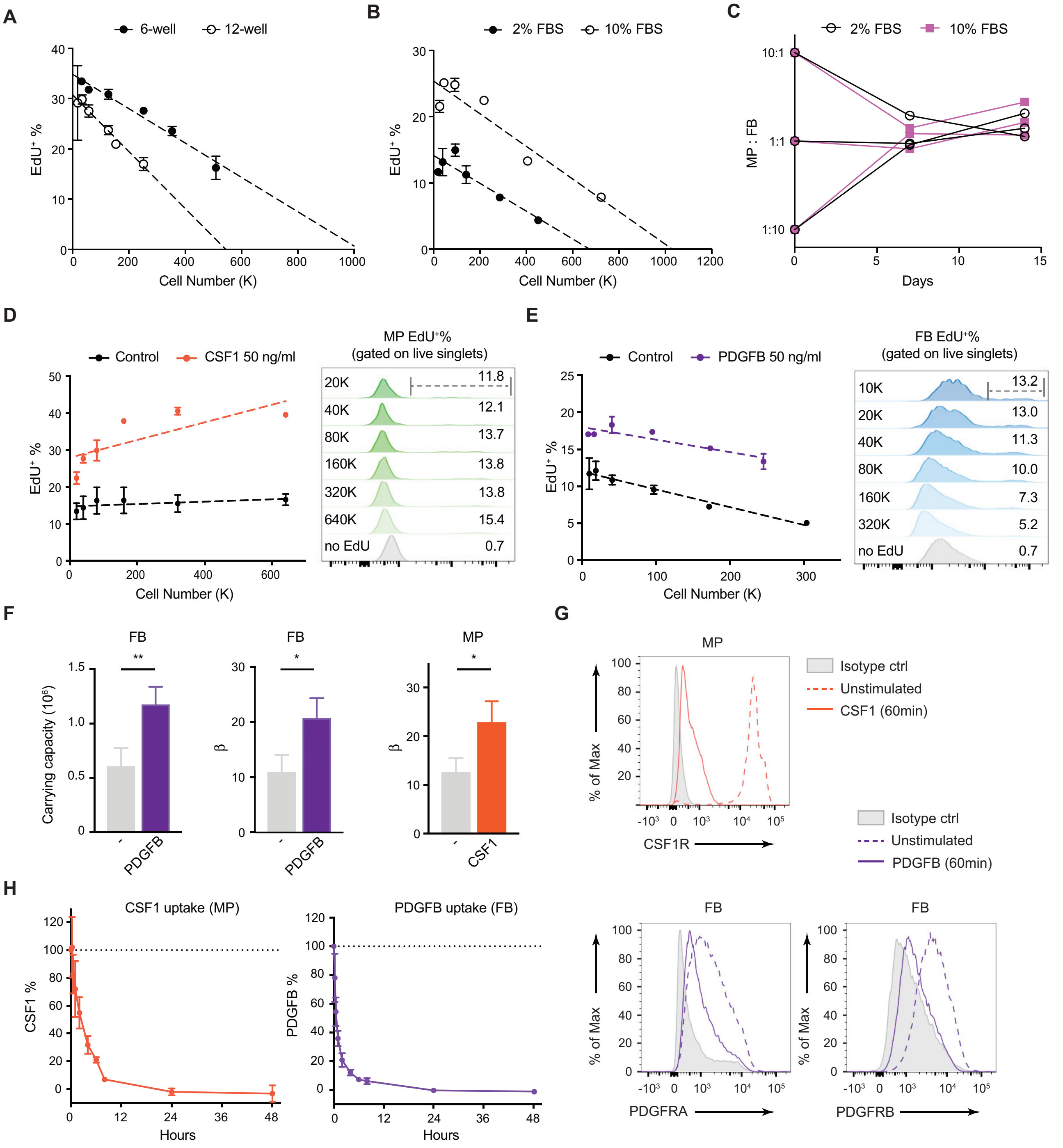

Figure S4. Carrying Capacity Is Regulated by Space, Nutrients, and Growth Factor Availability, Related to Figure 4

(A) EdU labeling of FB plated in 6-well or 12-well tissue culture plates at different cell densities, 320,000; 240,000; 160,000; 80,000; 40,000; 20,000 cells/well (6-well) and 160,000; 120,000; 80,000; 40,000; 20,000; 10,000 cells/well (12-well). FB were labeled with EdU for 2 hr after overnight culture in 2% FBS. Dashed line indicates linear regression of the data (data representative of two independent experiments, n = 2).

(B) EdU labeling of FB plated in 6-well tissue culture plates at different cell densities, 320,000; 240,000; 160,000; 80,000; 40,000; 20,000 cells/well. FB were labeled with EdU for 2 hr after overnight culture in either 2% or 10% FBS. Dashed line indicates linear regression of the data (data representative of two independent experiments, n = 2).

(C) MP:FB ratios 7 and 14 days after co-culture in either 2% or 10% FBS. Starting cell numbers were 10:1 (160,000 & 16,000), 1:1 (80,000 & 80,000), and 1:10 (16,000 & 160,000). (data representative of two independent experiments, n = 2).

(legend continued on next page)

(D) EdU labeling of MP stimulated with CSF1 at different cell densities. MP were labeled with EdU for 2 hr after the addition of PBS or 50 ng/ml CSF1 for 16 hr. Dashed line indicates linear regression of the data. Histograms show examples of EdU^+ flow cytometry gating for each cell density (data representative of three independent experiments, n = 2).

(E) EdU labeling of FB stimulated with recombinant PDGFB at different cell densities. FB were labeled with EdU for 2 hr after the addition of PBS or 50 ng/ml PDGFB for 16 hr. Dashed line indicates linear regression of the data. Histograms show examples of EdU^+ flow cytometry gating for each cell density (data representative of three independent experiments, n = 2).

(F) Effects of growth factors on FB and MP. Carrying capacity and proliferation rate (β) of FB with the addition of 50 ng/ml PDGFB, and proliferation rate of MP with addition of 50 ng/ml CSF1 for 16 hr were measured after 2 hr of EdU labeling (pooled data from three independent experiments). $^*p < 0.05$; $^{**}p < 0.005$, Student's t test.

(G) Surface expression of growth factor receptor measured by flow cytometry. Representative histograms of CSF1R, PDGFRA, and PDGFRB levels on either MP or FB at 60 min post growth factor stimulation (solid lines) compared to unstimulated cells (dashed lines).

(H) The uptake of recombinant CSF1 by MP and recombinant PDGFB by FB. 500,000 MP and 50,000 FB were plated in 12-well plates. Before the assay, MP were deprived of L929 medium supplement and FB were deprived of FBS for 16 hr. At the beginning of the assay, culture supernatant was sampled immediately after the addition of 10 ng recombinant growth factors (time 0), and then at 15 min, 30 min, 1 hr, 2 hr, 4 hr, 6 hr, 8 hr, 24 hr, and 48 hr. The concentrations of the remaining growth factors were quantified by ELISA and normalized to the concentration at time 0 (data representative of two independent experiments, n = 3).

Data are represented as Mean ± SD.

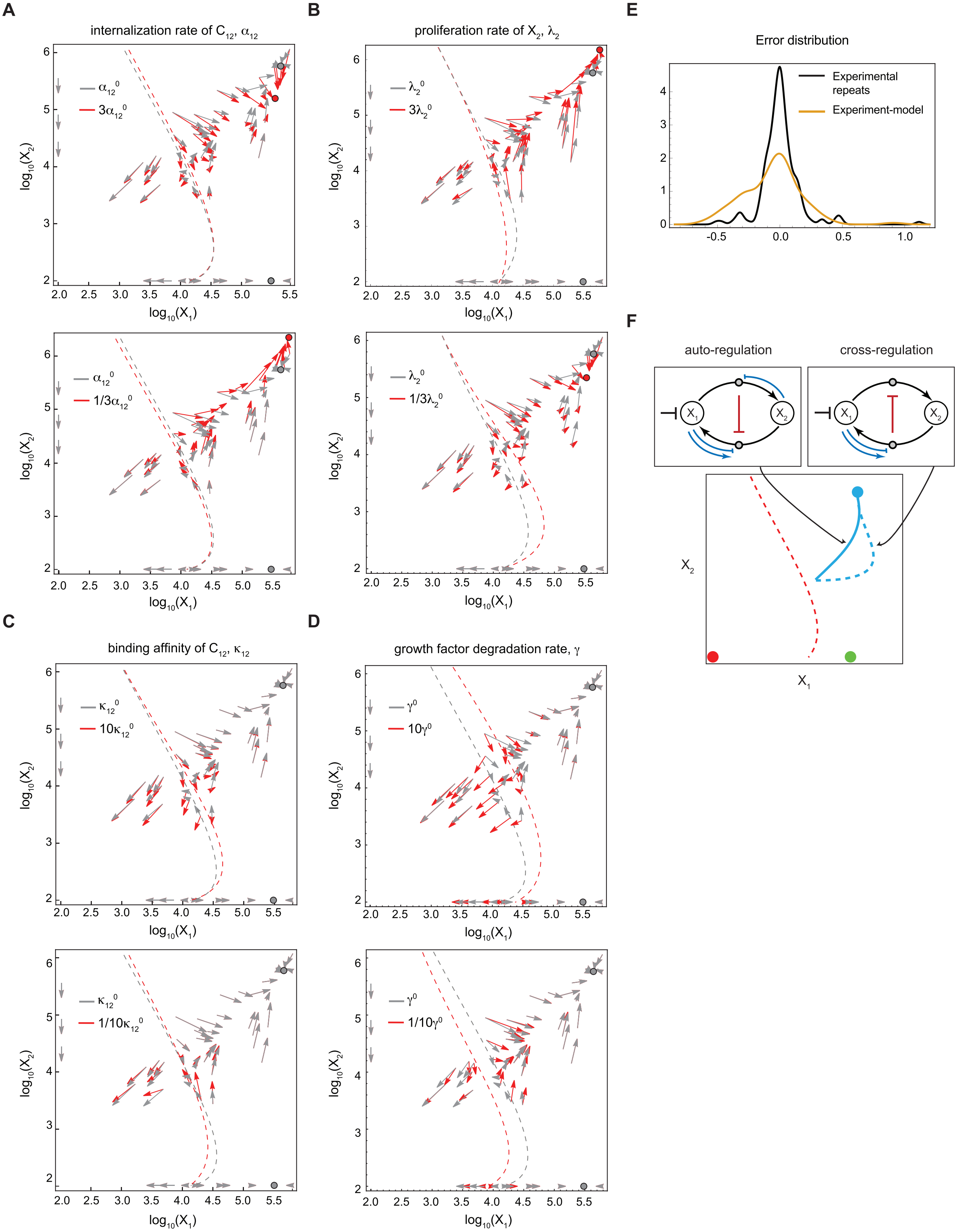

(legend on next page)

Figure S5. Cell Circuit Stability Is Robust to Changes in Model Parameters, Related to Figure 5

(A–D) Theoretical phase portraits showing the effects of varying model parameters. The calculated phase portrait with the biologically plausible parameter set, p^0 (Figure 5D; Table S2) is shown in gray. The phase portrait with internalization rate, α_{12}, with 3-fold higher (top panel) and lower (bottom panel) internalization rates (A), proliferation rate, λ_2 with 3-fold higher and lower (B), binding affinity, k_{12}, with 10-fold higher and lower (C), and degradation rate, γ, with 10-fold higher and lower (D) are shown in red. (E) Error distribution of biological repeats of FB and MP measurements shown in the phase portrait (Figure 5C) and the distribution of the deviation between the model and the experimental measurements. (F) Phase portrait depicting the difference in kinetics between auto-regulation and cross-regulation. In the presence of auto-regulation, the circuit flows more quickly to the stable 'ON' state (solid blue line) than in the presence of cross-regulation (dashed blue line).

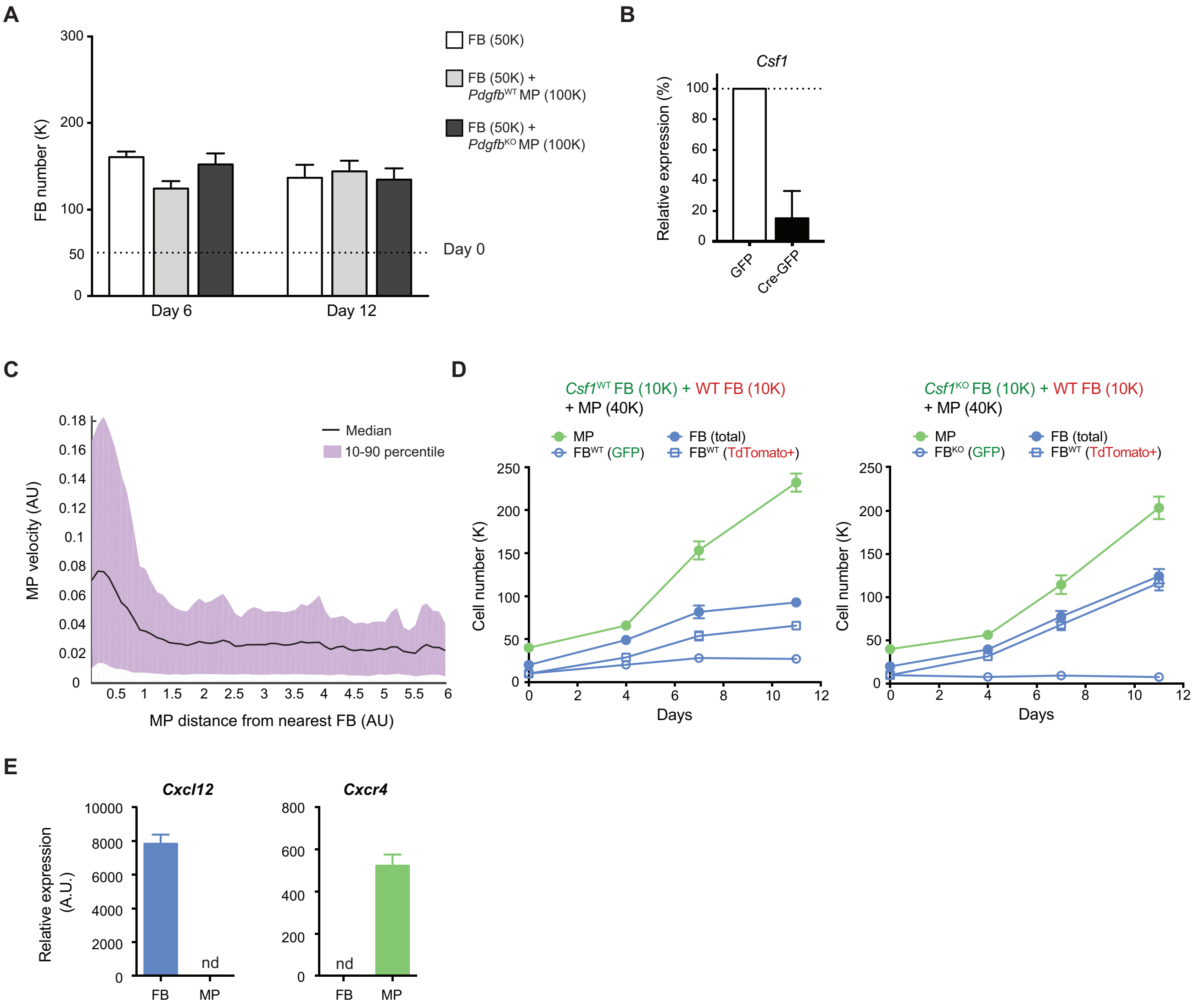

Figure S6. Macrophage and Fibroblast Stability in Co-culture Requires Cell-Cell Contact, Related to Figure 7

(A) Co-cultures of FB with *Pdgfb* WT or *Pdgfb* KO MP. Cas9-knock-in MP transduced with lentivirus carrying empty vector (control) or vector carrying *Pdgfb* guides (*Pdgfb* KO) were plated together with FB. On day 0, 50,000 FB and 100,000 MP were plated and the co-cultures were examined after 6 and 12 days (data representative of two independent experiments, n = 3).

(B) Expression of *Csf1* in FB transduced with lentivirus carrying either GFP (control) or Cre-GFP (*Csf1* KO). RNA expression was quantified by qPCR and normalized to *Rpl13a* expression. Pooled data from two experiments are shown.

(C) Live cell trace analysis of MP movement. Movement of MP in co-culture with FB is analyzed. The speed of MP movement is binned based on the minimal distance between MP and FB. 20,000 FB and 50,000 MP were plated and time-lapse imaging began 6 hr after plating.

(D) Number of GFP$^+$ (control or *Csf1* KO) FB, TdTomato$^+$ WT FB, total FB, or MP after co-culture. 10,000 *Csf1*$^{fl/fl}$ FB transduced with lentivirus carrying either GFP (control) or Cre-GFP (*Csf1* KO) were plated together with 10,000 TdTomato+ WT FB and 40,000 MP. Cells were harvested and analyzed by flow cytometry 4, 7, and 10 days after co-culture (data representative of two independent experiments, n = 3).

(E) Expression of *Cxcl12* and *Cxcr4* in MP and FB, quantified by qPCR and normalized to *Hprt1* expression, “nd” = not detected (data representative of two independent experiments, n = 3).

Data are represented as Mean ± SD.